EXPERIMENTAL REALIZATION OF A FEEDBACK RATCHET AND A METHOD FOR SINGLE-MOLECULE BINDING STUDIES

by

BENJAMIN J LOPEZ

A DISSERTATION

Presented to the Department of Physics
and the Graduate School of the University of Oregon
in partial fulfillment of the requirements
for the degree of
Doctor of Philosophy

December 2010

"Experimental Realization of a Feedback Ratchet and a Method for Single-Molecule Binding Studies," a dissertation prepared by Benjamin J Lopez in partial fulfillment of the requirements for the Doctor of Philosophy degree in the Department of Physics. This dissertation has been approved and accepted by:

Dr. Raghu Parthasarathy, Chair of the Examining Committee

Date

Committee in charge:
Dr. Raghu Parthasarathy, Chair
Dr. Heiner Linke, Research Advisor
Dr. Dan Steck
Dr. John Toner
Dr. Brad Nolan

Accepted by:

Dean of the Graduate School

An Abstract of the Dissertation of

Benjamin J Lopez for the degree of Doctor of Philosophy

in the Department of Physics to be taken December 2010

Title: EXPERIMENTAL REALIZATION OF A FEEDBACK RATCHET AND A METHOD FOR SINGLE-MOLECULE BINDING STUDIES

Approved: _____

Dr. Heiner Linke

Biological molecular motors exist in an interesting regime of physics where momentum is unimportant and diffusive motion is large. While only exerting small forces, these motors still manage to achieve directed motion and do work. Brownian motors induce directed motion of diffusive particles and are used as models for biological and artificial molecular motors.

A flashing ratchet is a Brownian motor that rectifies thermal fluctuations of diffusive particles through the use of a time-dependent, periodic, and asymmetric potential. It has been predicted that a feedback-controlled flashing ratchet has a center of mass speed as much as one order of magnitude larger than the optimal periodically flashing ratchet. We have successfully implemented the first experimental feedback ratchet and observed the predicted order of magnitude increase in velocity.

We experimentally compare two feedback algorithms for small particle numbers and find good agreement with Langevin dynamics simulations. We also find that existing algorithms can be improved to be more tolerant to feedback delay times. This experiment was implemented by a scanning line optical trap system.

In a bottom-up approach to understanding molecular motors, a synthetic protein-based molecular motor, the "tumbleweed", is being designed and constructed. This design uses three ligand dependent DNA repressor proteins to rectify diffusive motion of the construct along a DNA track. To predict the behavior of this artificial motor one needs to understand the binding and unbinding kinetics of the repressor proteins at a single-molecule level. An assay, similar to tethered particle motions assays, has been developed to measure the unbinding rates of these three DNA repressor proteins. In this assay the repressor is immobilized to a surface in a microchamber. Long DNA with the correct recognition sequence for one of the repressors is attached to a microsphere. As the DNA-microsphere construct diffuses through the microchamber it will sometimes bind to the repressor protein. Using brightfield microscopy and a CCD camera the diffusive motion of the microsphere can be characterized and bound and unbound states can be differentiated. This method is tested for feasibility and shown to have sufficient resolution to measure the unbinding rates of the repressor proteins.

CURRICULUM VITAE

NAME OF AUTHOR: Benjamin J Lopez

GRADUATE AND UNDERGRADUATE SCHOOLS ATTENDED:

University of Oregon, Eugene, Oregon
Pacific University, Forest Grove, Oregon

DEGREES AWARDED:

Doctor of Philosophy in Physics, 2010, University of Oregon
Master of Science in Physics, 2006, University of Oregon
Bachelor of Science in Physics, 2004, Pacific University

AREAS OF SPECIAL INTEREST:

Molecular Motors, Optical Trapping, and Biological Physics

PROFESSIONAL EXPERIENCE:

Graduate Teaching Fellow,
University of Oregon, 2004-2005
Graduate Research Assistant,
University of Oregon, 2006-2010
GK-12 Fellow,
University of Oregon, 2008-2009
IGERT Fellow,
University of Oregon, 2009-2010

GRANTS, AWARDS AND HONORS:

GK-12 Fellowship, 2008-2009

IGERT Fellowship, 2009-2010

PUBLICATIONS:

EHC Bromley, NJ Kuwada, MJ Zuckermann, R Donadini, L Samii, GA Blab, GJ Gemmen, BJ Lopez, PMG Curmi, NR Forde, DN Woolfson, H Linke. "The Tumbleweed: towards a synthetic protein motor." HFSP Journal 3 (2009).

BJ Lopez, NJ Kuwada, EM Craig, BR Long, H Linke. "Realization of a Feedback Controlled Flashing Ratchet." Physical Review Letters 101 (2008).

EM Craig, NJ Kuwada, BJ Lopez, H Linke. "Feedback control in flashing ratchets." Annalen der Physik 17 (2008).

ACKNOWLEDGEMENTS

Thanks to Heiner for guiding me through the long winding path that is research. Thanks for not losing confidence in me when it took way too long to get the optical trap working, and thanks for pushing me to write a decent thesis.

Thanks to Brian Long, Erin Craig, Nate Kuwada, Gerhard Blab, Greg Gemmen, Martina Balaz, Cassie Niman and everyone else in the group for answering questions, engaging in helpful discussions, and commiserating about the difficulties. Thanks to the collaborators Paul Curmi and Roberta Davies at UNSW for teaching me everything I know about protein expression and giving me a great excuse to spend a month in Sydney. Thanks to Jens-Christian Meiners and Raj Nambiar at University of Michigan for letting me visit and helping me get a handle on the details of the scanning optical trap system.

For emotional support that was absolutely necessary I thank Gabby and the rest of my family: my mom, sister, grandparent, aunts and uncles, cousins, everyone.

TABLE OF CONTENTS

Chapter Page

LIST OF FIGURES

Figure Page

Figure Page

Figure Page

CHAPTER I

INTRODUCTION

Biological molecular motors are of great interest in the biophysical research community. There are several motor proteins that have been characterized extensively. Models for the linear, processive, load carrying motors myosin and kinesin have been proposed [1, 2]. Due to these motors small size (on the order of ten nanometers) and aqueous environment, they exhibit interesting and unintuitive physics. At this size inertial forces are insignificant and random Brownian diffusive forces are large compared to the energy available to the molecules from ATP hydrolysis. Research into the physics of these motors has the potential to greatly increase our understanding of the biological function and the design traits that enable that function. This understanding could lead to the design of useful artificial nanomachines.

In this thesis, we begin with a discussion of the theory of Brownian motion (chapter II) and Brownian ratchets (chapter III) and how these topics relate to the research done for this thesis. Brownian motion is the constant jittering motion, diffusion, observed in micron scale and smaller objects in solution. A Brownian ratchet is a system that induces directed motion of diffusive particles. It does this without the use of an overall force, and the Brownian motion of the particle is a necessary part of the operation of the motor.

Next a technique called optical trapping (chapter IV) is explained due to its use in our feedback ratchet research described in chapter V. An optical trap uses the momentum transfer of light refracting through an object to confine that object. This can be done effectively with micron scale spheres in water. By scanning this trap in one-dimension, a line of light can be generated, and this line can trap a microsphere in two-dimensions while allowing it to freely diffuse in the other.

Brownian ratchets are most commonly operated without using information about the particle's current position. A feedback ratchet uses real-time information about the particle's position to improve ratchet performance, primarily the average speed of the particle. A large increase in particle speed has been predicted by theory. We successfully designed and implemented a feedback ratchet system through the use of a scanning line optical trap. This was the first experimental realization of a feedback ratchet system. We were able to use this system to test the performance of a feedback algorithm that maximized the instantaneous velocity (MIV method) of the particle and found an order of magnitude increase in particle speed compared to a ratchet without feedback. We proposed an algorithm that instead maximizes the net displacement (MND method) of the particle, and find that, because of the implementation delay time that occurs in experiment, the MND method increases the average particle speed compared to the MIV method.

In the next portion of this thesis biological molecular motors are described as well as our plans to make artificial molecular motors (chapter VI). This includes a

description of the "Tumbleweed" and "Inchworm" motors that are in development in this lab and with collaborators. Both of these motors are protein-based and use naturally occurring non-motor proteins as key components. The non-motor proteins used as components of both of these artificial motors are DNA binding repressor proteins. Each protein binds to a specific sequence of DNA, called an operator. The repressor proteins are ligand activated, which means they have a much stronger binding affinity to their operator DNA once the specific ligand has bound to the protein compared to the binding affinity when the ligand is not bound to the protein. The Tumbleweed (TW) connects three different repressor proteins to coiled-coil stalks that then connect to a central hub. It walks on a track of DNA made up of a repeating series of the three operator sequences. The Inchworm motor (IW) has a very different geometry. Two repressor proteins are immobilized on a surface to form a carpet. The motor itself is a length of DNA with an operator sequence at each end. The DNA is in a nanochannel, and in the nanochannel its length can be controlled by salt concentration. By correctly controlling the sequence of salt and ligand concentrations in solution, the inchworm motor would move unidirectionally.

To measure the binding rates of the repressor proteins, we developed a single molecule method. This method is a variation on tethered particle motion (TPM) experiments. In TPM a length of DNA is attached to a surface at one end and a diffusive microsphere at the other end. The diffusive motion of the microsphere can be observed by a brightfield microscope. Length changes of the tether are observed

by a change in the diffusive motion of the microsphere. In our assay, instead of observing changes in the length of the tether, we observe changes from diffusive motion to tethered motion; the microsphere is initially freely diffusing and then becomes tethered when the free end of the DNA binds to a repressor protein immobilized on the surface. This method allows us to measure the single-molecule unbinding times of the DNA repressor proteins that make up the TW and IW motors. While the original plan was to actually characterize the binding behavior of the proteins, due to time constraints the method has been tested for feasibility only. Included in chapter VII is the development of the single molecule method, a feasibility study, and a rationale for using a single-molecule type assay for this particular use. We find that the two states, freely diffusive and tethered, were able to be differentiated in experiment. By using a Page's test method of analysis, we find that the unbinding time can be measured to an accuracy of about 100 ms.

A detailed description of molecular biology methods used for the studies done in chapter VII are found in appendix A. The algorithms used for particle tracking in both the feedback ratchet experiment and the single-molecule assay are described in appendix B. Axial forces on microspheres due to optical trapping were calculated and this is described in appendix C.

The following variables, constants, and acronyms are used throughout the thesis:

- d: diameter
- r: radius

- g: acceleration of gravity at the surface of the earth, 9.81 m/s^2
- λ: wavelength of the laser light of the trap
- z-axis: optical axis, positive is in the direction of laser propagation
- γ: stokes drag coefficient. For a spherical particle $\gamma = 6\pi\eta r$
- η: viscosity
- k: Boltzmann's constant, $1.38 \times 10^{-23} J/K$
- T: temperature (K)
- α: control parameter, can be 0 or 1
- L: physical length of period
- MIV: maximization of instantaneous velocity
- MND: maximization of net displacement
- τ: implementation delay time

CHAPTER II

BROWNIAN MOTION

Brownian motion is an important aspect of the physics in all of the research done for this thesis. The Brownian ratchets described (chapter III) as well as the feedback ratchet implemented (chapter V) require Brownian motion to function. Biological molecular motors often take advantage of Brownian motion in their operation and the proposed artificial molecular motors also rely on Brownian motion to complete their cycles (chapter VI). The single-molecule method proposed and tested in this thesis (chapter VII) uses changes in Brownian motion to determine the binding states of DNA binding repressor proteins.

Brownian motion was observed in 1828 by a botanist named Robert Brown. He noticed that pollen grains suspended in water were in constant random motion. He also found that even nonliving material like soot exhibited the same effect as long as the particles were of similar size. He eventually came to the conclusion that this phenomenon had nothing to do with life [3].

Brownian motion is ultimately caused by collisions at the molecular level. These collisions happen randomly and transfer a very small amount of momentum, but occasionally enough collisions will happen in the same direction to produce a measurable movement of a larger diffusive particle (such as the pollen in Brown's experiment.)

In a fluid the frictional force is proportional to the velocity: $F = ma = -\gamma v$. The constant of proportionality is the viscous friction coefficient, γ. Given that relationship, the velocity, v, ignoring Brownian motion is: $v = v_0 e^{-(\gamma/m)t}$, where m is the mass of the water molecule. m/γ gives the characteristic time for the velocity to drop to e^{-1} of the starting velocity and no force except viscous fluid friction. This is the time scale where momentum is still relevant and for a micron scale polystyrene sphere in water is on the order of a hundred nanoseconds. For time scales larger than the characteristic time the diffusive motion can be interpreted as a random walk.

In a one-dimensional random walk the mean displacement is always zero, but the position after a random walk of many steps has a probability distribution. The probability of being exactly at the starting point is very low. We can instead look at the mean squared displacement for N steps, $\langle x_N^2 \rangle$. This quantity is equal to the number of steps times the square of the step length and if we define the diffusion constant of the walk as $D = L^2/(2t)$ then:

$$\langle x_n^2 \rangle = NL^2 = 2Dt, \tag{II.1}$$

where t is the time between each step. By using the diffusion constant, D, we eliminate any need to know the ultimate step size of the random walk [3].

Since we've established that diffusion is caused by the random collisions of thermal molecules with the diffusive particle, and that in a fluid there is a viscous drag (γ), then it might be suspected that the molecular cause of the viscous drag is related to the same random collisions. If we assume this is true we can easily find the relationship

between D and γ. Using the equipartition theorem we know that the squared speed of a molecule is related to its temperature and we can equate that to the square of the step length divided by the time between steps of the random walk:

$$v^2 = kT/m = (\frac{L}{t})^2. \tag{II.2}$$

For a particle with a constant force, f, in a viscous fluid, the particle has a terminal velocity of $v = f/\gamma$. From the random walk view, in between collisions a particle will undergo uniform accelerated motion $x = v_0 t + ft^2/(2m)$. Since this is a random walk the average v_0 will be zero, so $\langle x \rangle = (ft^2)/(2m)$. We can equate these velocities to find that

$$v = \frac{f}{\gamma} = \frac{ft}{2m} \tag{II.3}$$

and this means that

$$\gamma = \frac{2m}{t}. \tag{II.4}$$

If we use equations II.2 and II.4 and our definition for D, we find that

$$\gamma D = \frac{2m}{t}\frac{L^2}{2t} = \frac{mL^2}{t^2} = kT. \tag{II.5}$$

This result ($\gamma D = kT$) is the conclusion of one of Einstein's 1905 publications [4] and is known as the fluctuation-dissipation theorem.

CHAPTER III

BROWNIAN RATCHETS

The relatively new field of nanotechnology presents many difficult technical challenges. For objects at the nanometer to micrometer scale in solution the physics that determines their behavior is quite a bit different than our macroscopic experience prepares us for. Objects at this scale are never at rest. Molecular collisions cause constant Brownian motion. Momentum is insignificant over a time scale greater than or equal to microseconds because of Brownian motion. Given the goal of a working molecular motor, we cannot simply shrink a macroscopic motor and achieve the same results. Many motors rely on momentum to complete a cycle of movement. An internal combustion engine has a piston that is pushed by the expansion of gas. Once the gas stops expanding, the momentum of the piston enables it to finish the cycle and return to the starting position. This wouldn't work without momentum. Design principles must change entirely to deal with the problems of Brownian motion and possibly to use that motion as an advantage.

Brownian motors [5] induce directed motion of diffusive particles and are used as models for biological and artificial nanomachines (chapter VI). A Brownian ratchet is a simple, tractable example of a Brownian motor that is used to test the behavior of motors at this size. In a ratchet system an asymmetric potential profile, along with

a means to push the system out of equilibrium, is used to induce directed transport of micron-scale objects. A ratchet achieves transport in this way without the use of a macroscopic chemical gradient or force. The Brownian ratchet subfield explores the parameters and conditions necessary to achieve transport for diffusive scale objects where thermal noise plays a substantial role. In the coming paragraphs it is described why both of these conditions are necessary. The feedback ratchet system implemented in chapter V and feedback ratchet systems in general are a special class of Brownian ratchets. In this chapter background on Brownian ratchets is given using: a thought experiment by Richard Feynman, a few theoretical formulations of ratchets, and several examples of working experiments.

The Feynman lectures on physics are a transcript of his lectures during a general physics class. These lectures are well known among physicists for their intuitive, accurate descriptions of physical behavior, and for the way he shows the connections between different fields of science. His thought experiment of the ratchet system (figure 3.1) provides a really clear example of the second law of thermodynamics which states that in a closed system the entropy can only increase [6]. For a heat engine this means that there must be a hot and cold reservoir; that is the system can't be in equilibrium. In the ratchet system described by Feynman (figure 3.1) a rotor is in a thermal bath at temperature T_1 and is connected to a gear with asymmetrically ratcheted teeth. Loosely connected to the gear is a pawl that is sensitive enough to allow the gear to rotate due to thermal collisions. The gear and pawl are in a thermal

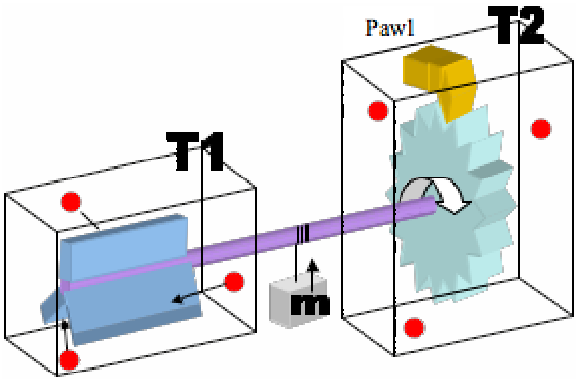

Figure 3.1. When the system is in equilibrium ($T_1 = T_2$) a Feynman ratchet does no work since the ratchet pawl is just as likely to lift off and allow rotation as the rotor is to be rotated by thermal fluctuations. When the system is out of equilibrium ($T_1 \neq T_2$) it becomes a simple heat engine and is able to do work. For the working macroscopic ratchet from ref. [7] there are changes made that break the symmetry of the system and push it out of equilibrium. Public domain image from: http://en.wikipedia.org/wiki/Brownian_ratchet.

bath at temperature T_2. Due to the asymmetric slope of the gear teeth the pawl is supposed to allow the gear to rotate in the direction of the shallow slope, but not in the direction of the steep slope side of the geartooth. At first glance it may seem that the rotor will have average rotation in one direction, even when $T_1 = T_2$. However since the pawl-gear connection must be weak enough to allow rotation of the rotor due to thermal motion of it, the pawl will undergo thermal motion as well. Because the pawl will lift off the gear frequently, it can be calculated that there will be no net rotation on average. If $T_1 \neq T_2$ then it is a normal heat engine and work can be done.

To understand the key conditions for a functioning ratchet, it is useful to start with an example. In a recent PRL article from Eshuis et al. [7], they make a few clever

changes to Feynman's example. The end result is that the setup actually functions as a Brownian ratchet.

The insight these authors had was a method to make this ratchet actually do work by converting the kinetic energy of a granular gas, composed of 4 mm glass spheres, into rotational motion of the rotor. A shaker agitates the granular gas which causes the glass spheres to strike the sides of the rotor. It is generally accepted that two conditions must be met to extract energy with a ratchet system: first the system must be out of thermal equilibrium, and second there must be some sort of asymmetry in the system. In this experiment the shaker agitates the spheres; this pushes the system out of equilibrium. The vanes are covered with rubber tape on one side (resulting in a different coefficient of restitution for each side of the vane), this provides the asymmetry of the system. This experiment also clearly shows that without either of these conditions, no work is done. Without the shaker the spheres don't hit the vanes, and nothing happens. Without the asymmetry of the vanes, the motion averages to zero [7]. As will be shown in the following examples of Brownian ratchets, these two qualities (out of equilibrium, and asymmetry of the system) are necessary.

Another type of Brownian ratchet, called a burnt bridges ratchet, involves a random walker on a one-dimensional lattice. As the walker passes discrete sections of the lattice it alters the lattice in such a way that the walker is unable to return to a section that has already been walked on. The motion is powered entirely by thermal fluctuations and rectification occurs, at the expense of chemical energy,

through the creation of asymmetric boundary conditions [8]. This type of ratchet has been proposed as a model for the motion of collagenase on collagen fibrils [9].

One formulation of a Brownian ratchet is to use an asymmetric sawtooth ratchet potential $V(x)$, with spatial period L (figure 3.2). The asymmetric requirement is fulfilled, but there will be no net motion as long as the system is in equilibrium. There are a couple methods that are used to push the system out of equilibrium. In a rocking ratchet [10, 11] there is an additional periodic force in addition to the sawtooth potential. This force averages to zero over time, but it pushes the system out of equilibrium as it cycles. For a flashing ratchet [12, 13] the sawtooth potential is turned on (control parameter $\alpha = 1$) or off ($\alpha = 0$). The sawtooth potential can be flashed randomly or periodically. If the potential is turned on and off periodically on the time scale of particle diffusion ($t = x^2/2D$) over the distance aL (figure 3.2) the mean particle velocity can reach up to the order of $L/2$ per flashing cycle ($\langle v \rangle = D/a^2L$). Just like the rocking ratchet, there is no overall force on the system

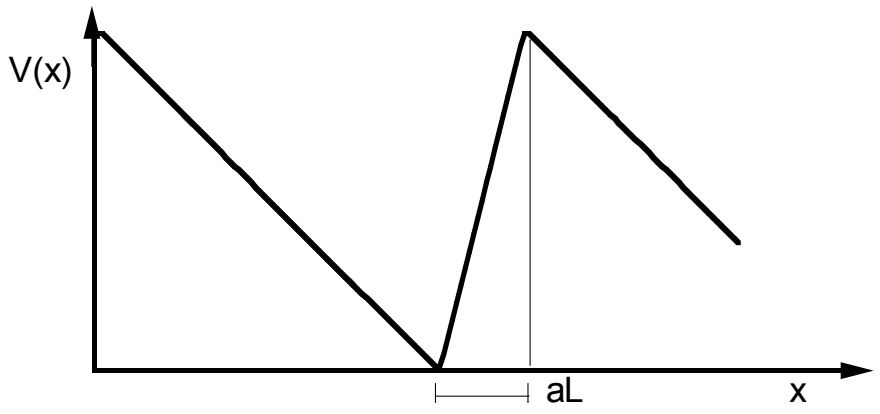

Figure 3.2. An example of a piece-wise, linear, asymmetric ratchet potential with asymmetry a and period L.

(i.e. tilt in the potential), but work can still be done. This doesn't break the second law because there is input energy. When the system switches from free diffusion to ratchet potential, particles in position x are raised to potential $V(x)$; this is the input energy.

Several experiments have been done that create functioning Brownian ratchets. A flashing ratchet with a circular, asymmetric sawtooth potential has been created by the use of a scanning optical trap [14, 15]. This setup was used to demonstrate a working flashing ratchet and compare its behavior to theory. Interdigitated electrodes with asymmetric spacing were used to transport short lengths of DNA [16]. These electrodes generated a potential similar to a sawtooth shape, and was also flashed on and off. A series of optical traps were created with a liquid crystal spatial light modulator [17]. By modulating the location of these traps over time a Brownian ratchet was created. Cold atoms have been trapped in optical lattices that are symmetric in space and time [18]. Asymmetry was created by having lattices that are out of phase with each other. This created asymmetric transfer rates for atoms transitioning between lattice points.

The field of Brownian ratchets has established some of the conditions that can be used to design a motor that functions at the nano and micro scale in an aqueous environment. The conditions described extensively in this chapter are spatial asymmetry and nonequilibrium of the system. As the previous paragraph demonstrates, Brownian ratchets have been demonstrated in experiment as well as in theory. What hasn't been

demonstrated experimentally are the results of using a real-time feedback controlled Brownian ratchet. We used a scanning line optical trap system to do this. Our results are described in chapter V.

CHAPTER IV

OPTICAL TRAPS

Optical trapping is the primary tool used to create the scanning line optical trap used to realize the feedback ratchet system. The feedback ratchet system makes up one of the two main topics of this thesis research. This chapter begins with a brief description of the history of optical trapping. It continues with enough theory of optical trapping to give the reader a qualitative understanding of it, with some idea of the difficulties of a quantitative calculation. The resolution limitations on an optical trap due to Brownian motion are then discussed and some of the experimental uses of optical traps are mentioned. The final section describes one-dimensional line optical traps in general and describes the specifics of the experimental setup we used to create a feedback Brownian ratchet.

History of Optical Trapping

Optical trapping takes advantage of the momentum of light, also known as radiation pressure. Limited to incoherent light sources, light momentum was considered significant only in the field of astronomy due to the huge intensities and long distances that are possible. After the invention of lasers, it became possible to have high enough intensities to create significant optical forces in the laboratory.

The possibility of optical trapping was understood when Arthur Ashkin did an order of magnitude calculation. The momentum of light is $p = E/c$, where E is the total energy of the light and c is the speed of light. For a perfectly reflective interaction the momentum change will be $2p$. Since force, F, is equal to $\Delta p/\Delta t$ and energy per time is power, P, then:

$$F = \frac{\Delta p}{\Delta t} = \frac{2p}{\Delta t} = \frac{2}{c}\frac{E}{\Delta t} = \frac{2P}{c}. \tag{IV.1}$$

For a one watt beam focused on a particle, diameter of one wavelength, this is a force of $\approx 10^{-8}$ N. Although this is a small force, the acceleration that it induces on a particle of that size in a vacuum is $\approx 10^5 g$, where g is the acceleration of gravity on the surface of the earth [19]. In water this force would result in a terminal velocity of $\approx 100\ \mu\text{m}/s$.

Ashkin did a simple experiment with latex spheres suspended in water. The expected velocity due to the radiation pressure of the laser was observed. However, there was an additional component of the force that hadn't been anticipated. There was a transverse force drawing the spheres toward the center of the beam, toward the region of highest intensity. [19]

Theory

Fig. 4.1 is a geometric optics diagram of the interaction between a Gaussian laser beam and a particle. This diagram shows refraction of the rays as they enter the

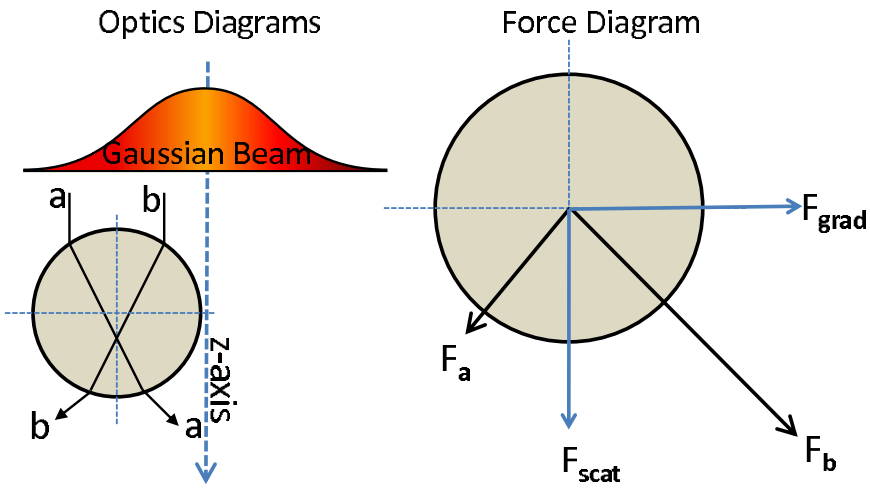

Figure 4.1. Optics Diagram: An off-axis microsphere interacts with a laser beam with a Gaussian intensity profile (TEM_{00} mode). Using geometric optics, the rays a and b refract through the microsphere as shown. The refraction of the rays imparts momentum on the microsphere. Force Diagram: since b has a higher intensity than a it imparts a greater force on the microsphere. The resulting force can be separated into a component in the direction of laser propagation, F_{scat}, and a component towards increasing beam intensity, F_{grad}. Figure adapted from [19].

spherical particle due to the difference of index of refraction between the particle and the medium. Ray a induces force F_a, and ray b induces force F_b. Since b is more intense than a, $F_b > F_a$. The net force can be separated into a component pointing in the direction of laser propagation, F_{scat}, and a component in the direction of increasing laser intensity, F_{grad}. [19] This is why the microsphere is attracted towards the center of the beam.

We can do even better than attraction towards the center of a Gaussian beam. Trapping in all three dimensions is possible with a focused laser beam. Fig. 4.2 is a geometric optics diagram of the interaction between a focused Gaussian laser beam and a spherical particle. Because of the different angle of incidence of the rays,

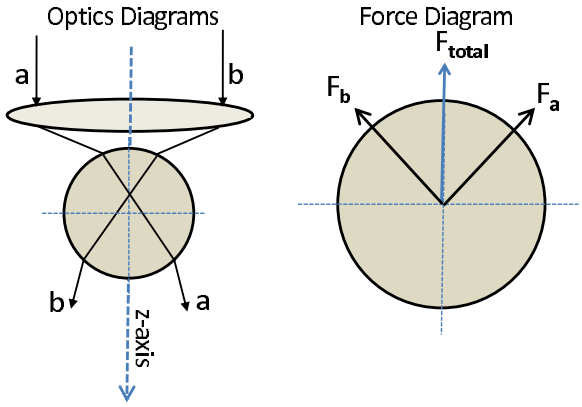

Figure 4.2. Optics Diagram: An on-axis microsphere interacts with a focused beam. Using geometric optics the, the rays a and b refract through the microsphere as shown. The refraction of the rays imparts momentum on the microsphere. Force diagram: Because of the large angle relative to the normal at which a and b hit the microsphere, the resulting force is opposite the direction of laser propagation (negative z-direction). Figure adapted from [19].

compared to fig. 4.1, there is a net force in the opposite direction of laser propagation towards the focal point of the laser beam. Because of the ability to trap in three dimensions, optical traps are also known as optical tweezers.

Although the geometrics optics explanations work qualitatively, they are not quantitatively accurate. Geometric optics is a good approximation only when the diameter, d, of the particle is much greater than the wavelength, λ, of the light ($d \gg \lambda$). In the case of 1064 nm light and micron sized beads, they are almost exactly the same size ($d \approx \lambda$). This also means that the point-dipole approximation isn't accurate ($d \ll \lambda$). To get the physics right it is necessary to use Mie scattering solutions which are complete analytical solutions to Maxwell's Equations for scattering of EM radiation by spherical particles [20]. It requires infinite sums of multipole terms, but by cutting off the sums at some accuracy limit, and by solving numerically, one can

come up with reasonable answers for forces on the bead due to the optical trap. (For an example of solving this for the value of axial trapping force, see appendix C.)

There have been detailed electric field calculations used to find the trapping forces of optical traps on dielectric spheres. The usual method is to represent the focused beam as a sum of plane waves [21–23]. These calculations have included index mismatches found in experimental setups [22, 23]. What is found from these calculations is that, because of the balance between F_{scat} and F_{grad}, the microsphere is trapped about 100 nm further down the z-axis than the focal point of the laser beam. Once index mismatches (immersion oil, glass, water) are included the optical trap potential is made wider, and shallower.

The common thread behind many of the biological experiments using optical point traps is the use of the trap as a force transducer. An optical trap is typically approximated as a Hookian restoring force ($F = -\kappa x$). Once the trap is calibrated and its position and κ are known, the force on a bead in the optical trap is also known. In many experiments the bead is coupled to some biological process exerting a force. This force is recorded by measuring the displacement of the bead from the center of the trap [24]. Optical traps are typically sensitive on the scale of 1 pN to hundreds of pN. This is a useful range of sensitivity since many biological systems have forces at this scale (described more in chapter VI). The relevant energy scale of Brownian motion is kT, the product of Boltzmann's constant and the temperature. For reference, this is approximately equal to 4 pN nm (piconewtons $\times$ nanometers).

At physiological conditions one ATP is converted to ADP to release about 20 kT (80 pN nm) of energy. Since molecular biological processes happen at the nanometer scale. 20 kT of energy results in forces in the measurable range.

The fundamental limit to the spatial resolution of an optical trap is the thermal noise of the diffusive particle in the trap. At any time the particle in the trap is balancing between three forces: the force due to the optical trap, the force due to the experiment being run (i.e. the tension on a DNA strand connected to the particle in a DNA stretching experiment), and the Brownian force of the surrounding medium. The experimental force being measured will always have this Brownian noise added to it. The signal to noise ratio, S/N, due to Brownian noise can be calculated as:

$$S/N = \frac{k_{tether}\Delta l}{\sqrt{4kTB\gamma}}. \tag{IV.2}$$

Where k_{tether} is the spring constant of the biological tether, Δl is the length of the displacement of the system, B is the bandwidth of the measurement, and γ is the drag coefficient of the bead. From this equation we can see that increasing k_{tether} improves the ratio. A stiffer tether better transmits information about the molecule it is attached to. Decreasing the particle size, which reduces γ, improves the ratio because a smaller particle diffuses faster which actually reduces measurement noise for a given bandwidth. Reducing temperature can also improve the ratio, but most biological systems are temperature sensitive, so this is not a desirable parameter to change [25].

Using back-focal plane interferometry it is possible to measure bead motion on the scale of ten nanometers with millisecond resolution [25]. A specific experimental setup and its associated noise greatly reduce this accuracy. Experimental noise can come from many sources: stage drift, mechanical vibrations in the setup, temperature fluctuations, pixel noise in a CCD camera, laser pointing and intensity fluctuations, etc. In a setup with two optical traps holding two beads tethered by a length of dsDNA, 3.4 angstrom steps at one second per step were able to be measured [25]. This allowed a measurement of single-base pair motion of an RNA polymerase. Interestingly, the trapping strength is not a factor in this relationship. Even though a stronger trap reduces the Brownian motion of the trapped particle, it also reduces the particle's sensitivity to the biological process being measured. Those two effects cancel each other out [25].

Many uses for optical traps have been devised. They have been used for trapping of live cells [26, 27], to create femtoliter aqueous droplets [28], to probe the mechanical properties of biological materials such as: DNA [29], and actin and microtubules [30]. Optical trapping techniques have been extensively used in the field of molecular motors to measure: RNA polymerase base stepping [31], stepping characteristics of kinesins [32, 33], myosins [34, 35], dyneins [36], and even the stochastic tug of war between kinesin and dynein on microtubules [37]. In the field of statistical physics, they have been used to study: colloidal transport [19, 38, 39], Brownian motion [40], and Brownian ratchets [17].

One-dimensional Optical Traps

An extension to the optical tweezers technique is to stretch the optical trap into a line to create a one-dimensional trapping potential along a micrometer scale length. This has been achieved in a number of different ways. Perpendicular galvonometer controlled mirrors can be used to generate a circular trap. This geometry allows a continuous track for particles trapped within it. Circular traps have been used to study single file diffusion [41] and flashing ratchets [14]. A cylindrical lens can be used to spread the laser beam in one direction. This has been used to study short-range colloidal interactions [42]. With the careful application and calibration, a phase-only holographic mask can be used to create a line trap [38, 43]. A line trap created by this method has been used to measure the pair interaction energy of lipid bilayer functionalized silica microspheres [44].

In general a line trap is created by scanning a focused laser beam in one dimension. The laser is scanned back and forth periodically and rapidly enough that the trapped bead feels a time averaged optical potential. If the trap is scanned very slowly the bead follows along with the trap. If it is scanned fast enough the bead feels a kick each time the trap passes by. As the scan speed is increased this kick gets smaller and smaller but never disappears entirely [15]. To explain this more thoroughly, consider a trap that scans at a certain speed, v_{trap}. It exerts a force, F, on the microsphere as it passes. This force gives the microsphere a terminal speed in solution, $v_{\text{sphere}} = F/\gamma$,

where γ is the viscous friction coefficient. If $v_{\text{trap}} \leq v_{\text{sphere}}$ then the bead follows along with the scanning trap. If $v_{\text{trap}} > v_{\text{sphere}}$ then the bead receives a kick but does not follow along with the trap. We can estimate the distance that each kick moves the microsphere. In this situation, the trap is passing over the microsphere as it scans. The time that they overlap is twice the radius of the microsphere divided by the difference in velocities: $2r/\left(v_{\text{trap}} - v_{\text{sphere}}\right)$. During this time the microsphere moves at a speed of v_{sphere}, so the kick distance is: $2rv_{\text{sphere}}/\left(v_{\text{trap}} - v_{\text{sphere}}\right)$. This calculation makes some simplifying approximations. It approximates the trap as a point, and it assumes the trap gives a constant force as it scans over the microsphere.

An acousto optic deflector (AOD) can also be used to scan a laser in one-dimension linearly. An AOD uses the acousto-optic effect. In this effect a sound wave in a crystal changes its refractive index. The high and lower pressure regions that the sound wave sets up in the crystal cause a similarly varying index of refraction. This changing index of refraction works as a diffraction grating and diffracts an incoming laser beam. Increasing the intensity of the sound wave increases the size of this effect. With this device the first order diffraction peak is used and by altering the frequency of the sound wave, the angle that this peak leaves the device can be altered within a small range (milliradians) to scan the laser. If the scan speed and light intensity are kept constant the microsphere can freely diffuse in one-dimension. This has been used to study entropic interactions [45] and single file diffusion of colloids [46]. By modulating the light intensity linearly within each scan, one can create a constant-

force measuring tool for single molecule experiments [29, 47]. If an AOD is used to create a ratchet like potential profile (i.e. figure 3.2) one can make a time-dependent flashing ratchet [14]. By adding feedback control, we can realize an experimental version of a feedback Brownian ratchet system. This is the topic of the next chapter.

Experimental Setup

We designed and implemented an AOD based scanning line optical trap for use in feedback ratchet experiments. A thorough description of the setup follows. A description and diagram of the optics setup is described in figure 4.3.

To create our optical trap, we used an oil immersion microscope objective (100x, 1.4 NA, Leica Model No. 11566014) to focus the beam into a microchamber. The microchamber is made using a coverslip, a microscope slide, and a piece of double-sided tape. The microscope slide has two small holes drilled through it and the tape has a small channel cut out of it that spans the distance between the two holes. When the slide, tape, and coverslip are sandwiched together this leaves a small channel (about 2 cm by 2 mm) that can be filled with solution using the holes in the slide. The tape thickness determines the thickness of the channel and is about 60 μm. Silica spheres, 0.9 μm diameter are used in these experiments. They are injected in solution into one of the input holes of the microchamber using a syringe. For all experiments discussed in this thesis the line trap is 17.4 μm long and the potential profile used contains ten ratchet periods ($L = 1.74$ μm). An image of the

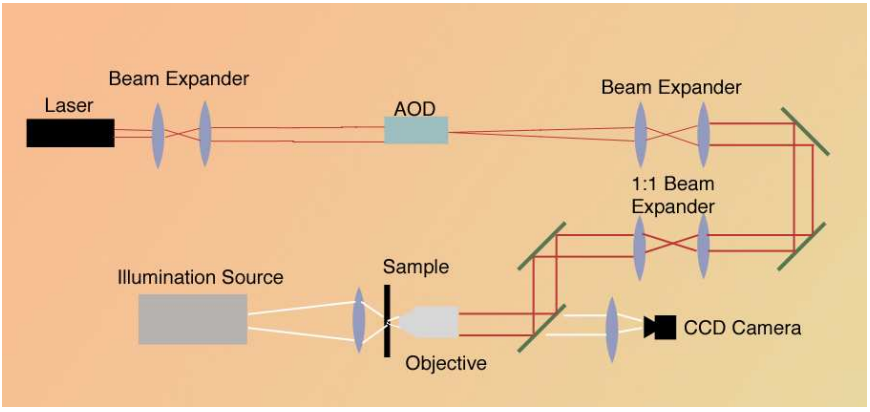

Figure 4.3. A telescope expands a 1 mm diameter 1064 nm wavelength laser to a beam diameter of 6.4 mm for the back aperture of the AOD. The AOD scans the laser beam in one-dimension which then goes through a second beam expander that reduces beam diameter to 5.6 mm for the back aperture of the microscope objective. A 1:1 expander is used for fine adjustment of the trapping beam. The microscope objective focuses the laser to a small point inside a microchamber. Brightfield illumination is used to image the sample on a CCD camera.

laser intensity representing this potential profile is shown in figure 4.4. Up to $N = 3$ spheres are trapped at a time.

Brightfield images (200x50 pixels) are captured by a CCD camera at 130 Hz and are analyzed through LabVIEW software to find the positions of the spheres (see appendix B for details of tracking algorithm), and a feedback algorithm is then applied. The implementation delay time for our experimental setup includes the time necessary to track the particle, apply the feedback algorithm, and to switch between potential shapes. The particle tracking software takes 4 ms to find the position of the particle from the image, and the feedback algorithm takes a negligible amount of time to be calculated. The potential shape is switched between flat and ratchet (see figure 4.4) by changing the state of a solid state relay; the relay has a response time

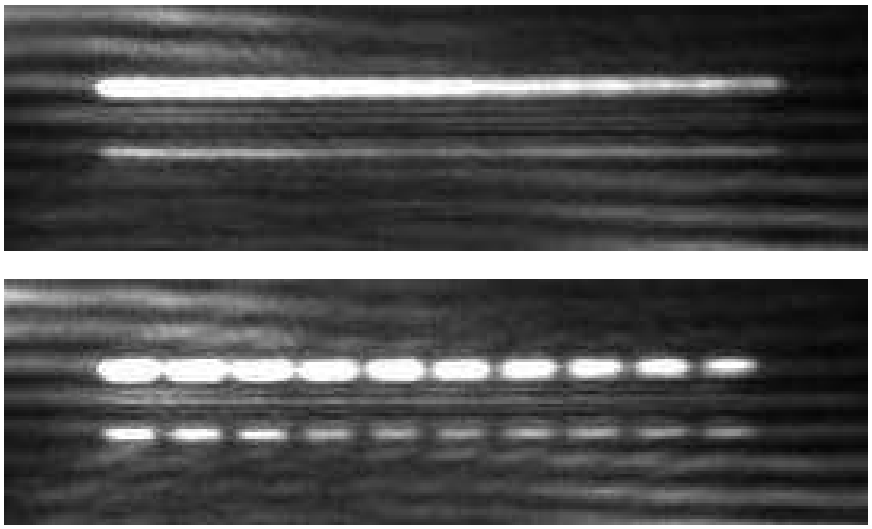

Figure 4.4. Top image: laser intensity at CCD camera for unmodified laser intensity scanned in one dimension using an AOD. Line length is 17.4 μm. Bottom image: Same scan using AOD, but now with laser intensity being modified within each scan to generate an asymmetric ratchet potential. For both images the optics setup created a dimmer reflection of the laser intensity that is seen as the lower line in each image.

of ≈ 1 ms. Therefore, the total implementation delay time is $\tau = 5$ ms, much less than the time scale of about 300 ms for bead diffusion over a distance aL, which has been found to be the upper limit for tolerable feedback delay for $N = 1$ [48].

To define a potential shape, a periodic signal is sent to the AOD via a function generator. To reduce the effects of the scanning kick, in this experimental setup the trap is scanned back and forth so that over one scan there should be both a forward and backward kick that cancel each other out. When scan speed and light intensity are kept constant the trapped bead is only allowed to undergo free diffusion in one dimension, along the scan direction. Since a trapped particle feels a force in the direction of higher intensity, a potential minimum is created by higher intensity light; a potential maximum is created by lower intensity light. The resulting output light

from the AOD will not perfectly match the signal sent by the function generator. There are two reasons for this. First, the AOD output is not uniform across its entire angular range. It varies in a way that is specific to each crystal. Second, the limited resolution of the AOD will act to smooth out the profile shape sent from the function generator. For this reason it is necessary to measure the resulting optical potentials and iteratively make corrections and re-measure the resulting potential until an accurate enough potential is measured.

CHAPTER V

FEEDBACK RATCHET

Feedback control of Brownian systems is useful to explore the limits of ratchet systems. By using real-time information about the system one can improve the performance of the ratchet immensely. Active real-time control allows us to use more information about the system than ensemble averages; we can use the fluctuations that disappear in the averaging process. Clever feedback algorithms can be compared and can exhibit complex, unexpected behaviors. This chapter presents the original research done for this thesis with an experimental realization of a feedback ratchet system. The chapter begins with the basic theory of feedback ratchets, and goes into detail about the experimental setup used to create this system. Several algorithms for feedback control were tested and their performance with the experimental system are compared to theoretical predictions.

Theory

If the goal of feedback control is to maximize the time-averaged center of mass velocity, $\langle v \rangle$, for one particle this is trivially simple. For the ratchet potential shown in figure 5.1 the average direction of transport for random flashing is to the right. To maximize $\langle v \rangle$ one should have the ratchet turned on ($\alpha = 1$) when the particle is on

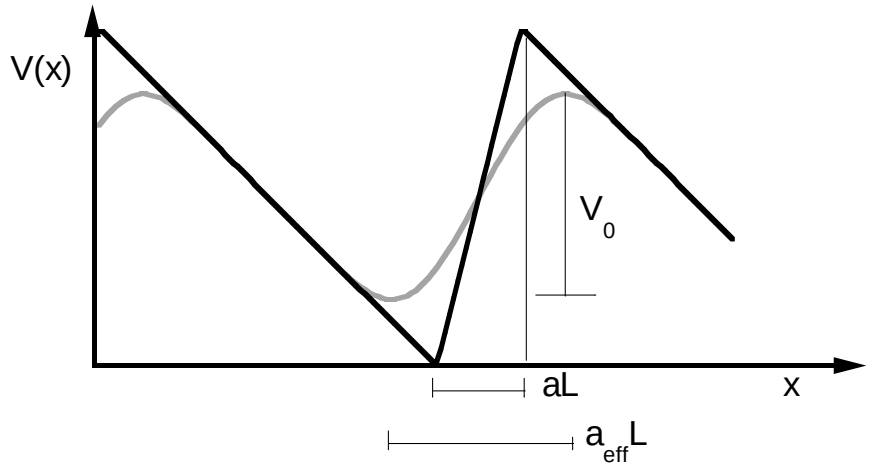

Figure 5.1. Black: a piece-wise linear ratchet potential $V_{lin}(x)$ with asymmetry $a = 0.2$ and period L. Gray: The effective potential $V_{\text{eff}}(x)$ (equation V.10) experienced by a sphere of radius $L/2$ trapped in $V_{\text{lin}}(x)$ has a reduced asymmetry $a_{\text{eff}} = 0.34$, and a reduced potential height V_0. In the text the downward sloping portion of the ratchet starting on the left going to the minimum is referred to as the "long side of the ratchet". The portion sloping upwards to the maximum is referred to as the "short side of the ratchet."

the long side of the ratchet, and the ratchet should be turned off ($\alpha = 0$) when the particle is on the short side of the ratchet. α is the control parameter determining if the ratchet potential is on (confining the diffusive particles) or off (allowing the free diffusion of these particles). For more than one particle the best solution is not as obvious or simple. For example, if $N = 2$ and there is one particle on the long side of the ratchet and one on the short side of the ratchet, is it better to have the ratchet on so that they both move towards the same minimum, or is it better to have the ratchet off to allow the particle on the short side to have an opportunity to diffuse past the barrier to the next period?

The first, most direct solution to maximize $\langle v \rangle$ for $N > 1$ could be to maximize the instantaneous velocity of the particles. There is a specific feedback algorithm that does this. It maximizes the instantaneous velocity (MIV) of overdamped particles by setting the control parameter α such that the net force on the particles is always zero or positive [49]:

$$\alpha = \Theta\left(\sum_{i}^{N} F\left(x_i\right)\right) \text{ (MIV)}. \tag{V.1}$$

Here Θ is the Heaviside function, $F(x_i)$ is the force on each particle if the ratchet potential was turned on, and x_i is the particle position. For small N this scheme results in a $\langle v \rangle$ an order of magnitude larger than in an optimally operated, periodically flashing ratchet [49]. Optimally operated means to flash the ratchet with the period that provides the largest $\langle v \rangle$. As N grows the increase in $\langle v \rangle$ compared to the optimal periodic flashing decreases until $N \approx 10^3$ when the MIV method is slower than optimal periodic flashing. As N gets larger the system becomes more deterministic. It takes a longer time for the distribution to equilibrate and the switching of α slows down greatly.

Instead of waiting for this to happen, $\langle v \rangle$ can be increased by making a change to the MIV method. By adding thresholds to the MIV method [50], $\langle v \rangle$ is equal to the MIV method at small N, equal to optimal periodic flashing at large N and slightly better than both in an intermediate range. The threshold strategy is more complex:

$$\alpha = \left\{ \begin{array}{l} 1 \text{ if } F(x) \geq \mu_{on}, \\ 1 \text{ if } \mu_{off} < F(x) < \mu_{on} \text{ and } \dot{F}_e xp(x) \geq 0, \\ 0 \text{ if } \mu_{off} < F(x) < \mu_{on} \text{ and } \dot{F}_e xp(x) < 0, \\ 0 \text{ if } F(x) < \mu_{off}. \end{array} \right\} \tag{V.2}$$

The threshold strategy is more successful because it uses the majority of the motion induced by the ratchet, and doesn't wait for the long tail of full equilibration required by the MIV method.

The MIV method considers the force on the particles. This means that a particle on the steep side of the ratchet is more heavily weighted than a particle on the shallow side of the ratchet, because the value of the force on the steep side is greater than the value of the force on the shallow side. It could improve the performance of the ratchet more to use a feedback scheme based on the net displacement of particles due to the ratchet potential. To this end, we proposed a feedback scheme called the maximization of net displacement method (MND). It has been predicted to give a moderate improvement on the performance of the ratchet (in comparison to the MIV scheme) for small $N > 1$ [51]. This scheme maximizes the net displacement of the particles by following this algorithm:

$$\alpha = \Theta \left(- \sum_{i}^{N} (x_i - x_0) \right) \text{ (MND)} \tag{V.3}$$

where x_0 and x_i are measured with respect to the potential minimum within each period of the potential, and x_0 is a reference point. In a perfect feedback system with

$N = 1$ and no experimental complications, $x_0 = 0$ would be the most direct way to implement the MND method. In a real implementation of feedback, it is not so simple. Feedback implementation delay could necessitate a nonzero value for x_0. The effects of shifting x_0 will be shown in a later section.

Realistic feedback implementations [48, 51] will need to take into account delays [48, 52, 53] in the implementation of feedback, as well as errors [54, 55] in the measurement of particle positions and forces. Interestingly synchronization effects [48] can occur that have an effect very similar to the thresholds. The synchronization effects occur with large N and significant implementation delay. The implementation delay time can make the feedback occur during a later cycle than it was intended since large N systems are nearly deterministic. The system behaves as if it had a much shorter implementation delay time and is almost identical to the threshold method.

Theory predicted, using the MIV method, that the performance of a flashing ratchet can be dramatically improved by an order of magnitude [49]. This theory doesn't take into account the measurement error and implementation delay time that are unavoidable factors in experimental implementations. A calculation can be done to consider these factors and determine if we still can expect to observe a significant velocity increase in experiment. In a feedback flashing ratchet system the probability of making the wrong feedback decision can be calculated as the portion of a Gaussian function that extends into a region where the feedback algorithm would result in a different value of α. For example (considering the MIV algorithm) in figure 5.2, given

a measured position, there is a normal distribution with a width, σ, determined by the expected measurement error where the particle may actually be. The distribution is centered at the measured position. By summing the portions of the distribution that fall outside of the dashed lines in figure 5.2, one can find the probability of making the wrong decision. If we truncate this sum to only the nearby periods of the ratchet (a good approximation for small measurement error), then this probability can be calculated as:

$$\begin{aligned} p(\sigma) =& \frac{1}{\sqrt{2\pi\sigma}} \int_a^1 \left(\int_0^a exp\left(\frac{-(t-x)^2}{2\sigma^2} \right) dt + \int_1^{1+a} exp(\frac{-(t-x)^2}{2\sigma^2}) dt \right) dx \\ &+ \frac{1}{\sqrt{2\pi\sigma}} \int_0^a \left(\int_{a-1}^0 exp\left(\frac{-(t-x)^2}{2\sigma^2} \right) dt + \int_a^1 exp(\frac{-(t-x)^2}{2\sigma^2}) dt \right) dx. \end{aligned} \tag{V.4}$$

The first line of this equation integrates, for all measured positions on the short side of the ratchet period, the portion of the distribution that extends into the long side of the ratchet period. The second line of this equation integrates, for all measured positions on the long side of the ratchet period, the portion of the distribution that extends into the short side of the ratchet period. For 10 nm position uncertainty, $L = 1.74$ μm, and $a = 0.35$, this equation gives: $p = 0.01$. This means that the probability of calculating the wrong α due to measurement error is 1%. This calculation can also be used to take into account implementation delay, that is the delay between making a measurement and acting on the system. For 5 ms implementation delay, using $\sigma = \sqrt{2Dt}$, $p = 0.06$. This gives a roughly 7% total chance of making the wrong feedback decision. How much does this reduce the velocity gains expected from feedback compared to a periodic ratchet? This can be determined by using the average information content

[55],

$$I = H(q) - H(p) \tag{V.5}$$

where H is the binary entropy function, and q is the probability that the corrupted value of α is zero:

$$H(x) = -xlog_2x - (1-x)log_2(1-x) \tag{V.6}$$

$$q = (1-p)b + p(1-b) \tag{V.7}$$

and b is the probability that $\alpha = 0$ and is a complicated function of p, V_0, and a (see ref. [55] for details). The square root of I determines an upperbound of the velocity compared to what is achievable with perfect position accuracy and zero implementation delay. Using the experimental parameters given before this results in an upper bound of 79% of the possible feedback velocity. Since an order of magnitude increase compared to the periodic flashing ratchet is expected, we should still be able to measure a significant improvement in transport with feedback.

Characterization of Optical Potentials

Before doing ratcheting experiments, we need to know what the flat and ratchet potentials that we are trying to create actually look like; we need to know how close they are to the flat and ratchet shapes used in theory.

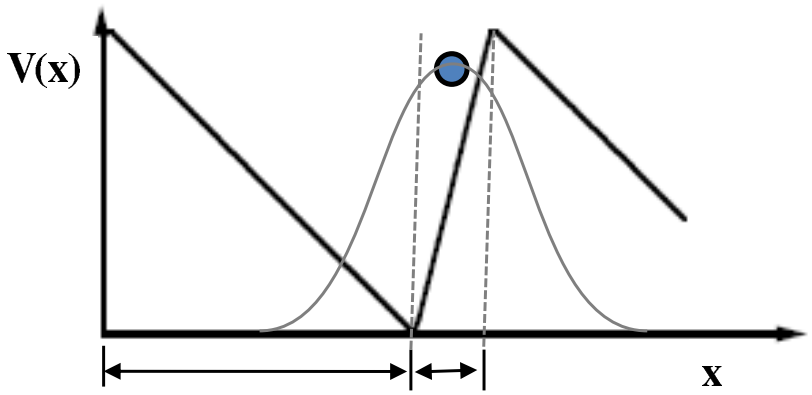

Figure 5.2. With a measured position as shown, the real position of the microsphere is represented by a normal distribution with a width determined by experimental measurement error. For the portion of the distribution within the gray dashed lines, the measured position gives the correct value of α. For the portion of the distribution outside of the gray dashed lines, the measured position gives the incorrect value of α. In the text, the short side of the ratchet period refers to the portion within the gray dashed lines, and the long side of the ratchet period refers to the portion to the left of the leftmost gray dashed line.

To characterize the flat potential (figure 5.4), we collected data of particles undergoing free diffusion in the one-dimensional trap and determined the potential from

$$V(x) = -kT \ln\left(\frac{N(x)}{N_{total}}\right) \tag{V.8}$$

where k is Boltzmann's constant, T is temperature, $N(x)$ is the number of data points at position bin x, and $N_{total} \approx 10^5$ is the total number of data points. We achieved a potential that was flat within one kT and stable over the course of weeks. This was accomplished by repeatedly measuring the effective potential and making adjustments to the input function to compensate for deviations from the desired flat potential shape (figure 5.3).

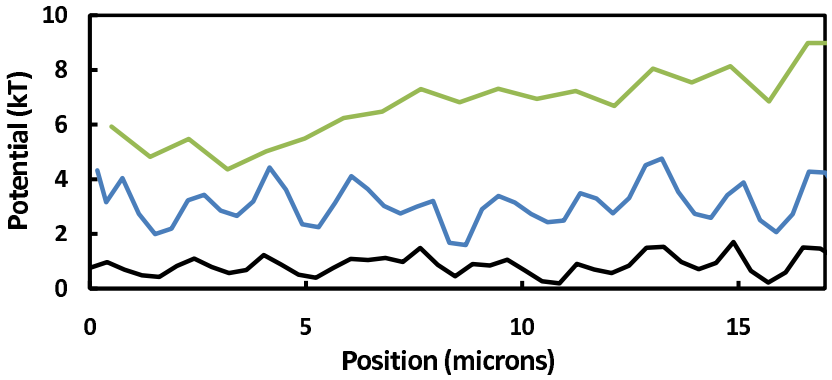

Figure 5.3. The top curve (green) is the measured potential with the AOD scanning a 17.4 μm line with a DC input function. There is an overall slope to the left, resulting in particles moving in that direction preferentially. The first step in correcting the potential was to compensate for that slope. The middle curve (blue) shows the measured potential after compensating for the overall slope. The slope is gone, but the fluctuations within the line are significant. The bottom curve (black) shows the final measured flat potential. The fluctuations in the line could be reduced, but not entirely eliminated.

Using the population method (equation V.8) relies on the Brownian motion of the microsphere to explore the potential. Because of this, excursions of more than a few kT from the bottom of a well are rare, and good statistics near the maxima of the ratchet potential can't be achieved. To measure the ratchet potential we also use

$$V(x) = -\gamma \int_0^x \bar{v}(x')dx' \tag{V.9}$$

where $\gamma = kT/D$ is the drag coefficient of the microsphere ($D = 0.44\ \mu\text{m}^2/s$ as measured), and $\bar{v}(x')$ is the ensemble average of the instantaneous velocity of the beads at position x'. To characterize the ratchet potential we use both of these methods and merge the results. The results are merged by matching the slopes of the potential shape near the minima. The resulting measured potential shape is shown

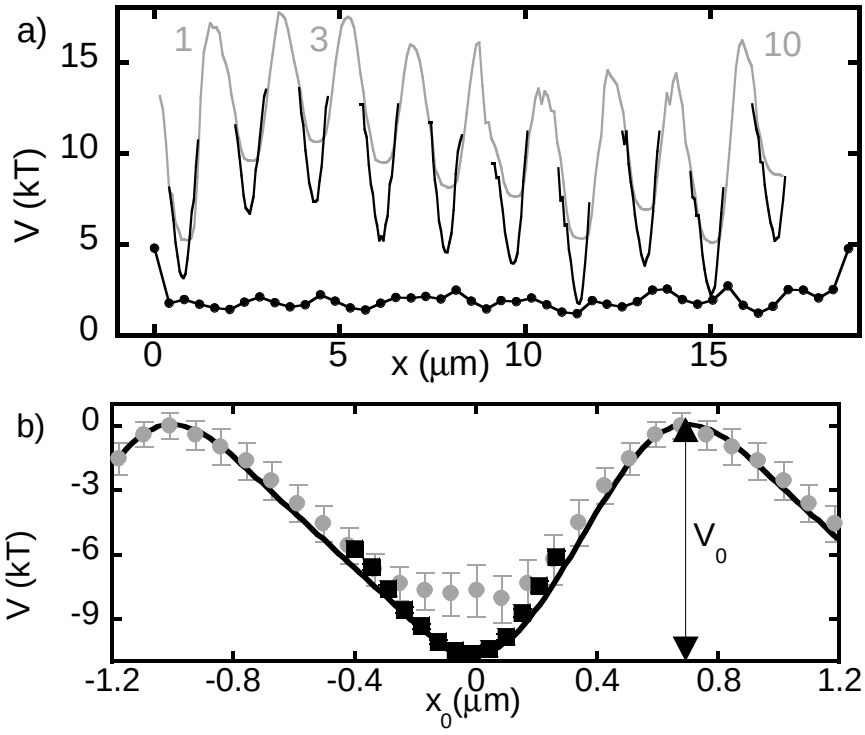

Figure 5.4. (a) The measured flat potential (black circles indicate experimental error) and the ratchet potential measured using equation V.8 and equation V.9 (black and gray lines, respectively, also in (b)). (b) The measured ratchet potential, averaged over all ten periods, yields $a_{\text{eff}} = 0.35 \pm 0.02$, and $V_0 = 10.6 \pm 0.3\ kT$, compared to $V_{\text{eff}}(x)$ (black line) calculated from equation V.10, using $a = 0.2$, $R = L/2$.

in figure 5.4. The input function generator shape used as input to the AOD was V_{lin} with $a = 0.2$. The error bars on the potential shape determined from the velocity method (equation V.9) are significantly larger than on the population method. This is due to a larger standard deviation in the measurements of the particle velocity compared to the standard deviation in the measurements of the position. The only way to get a smooth, continuous potential profile is to match the two methods on the slopes as described.

As can be seen in figure 5.4, the measured potential is quite a bit different than the piece-wise linear potential that was input to the AOD. In previous paragraphs it was mentioned that AOD resolution and non-uniform output over the scanning range can cause a difference between the input and the output. There is another factor to consider. What is being measured with population and velocity methods are not the intensity of the light at a single point. What is being measured is the microsphere's reaction to the line trap; this is the effective potential. The microsphere doesn't sample a single point of the laser profile intensity. It samples over its entire diameter. A finite-size sphere of radius R spatially averages over a given one-dimensional ratchet potential $V(x)$ and experiences the effective potential

$$V_{\text{eff}}(x, R) = \frac{3}{4\pi R^3} \int_{x-R}^{x+R} V(x')S(x')\,\mathrm{d}x' \tag{V.10}$$

where $S(x')$ is the cross-sectional area perpendicular to the ratchet direction of the bead at position x'. The effective potential calculated using the above equation for V_{lin} with $a = 0.2$ is shown in figures 5.1, and 5.4. Since we don't have the ability to measure the potential height of the original V_{lin}, the height of V_{eff} in fig. 5.4b is fit to match the measured potential. The shape of V_{eff} from eq. V.10 matches the measured potential very well.

Results

To accurately measure the effects of the feedback algorithms, the experiment must be performed carefully, to not create any unintended biases. For example, for our

measured ratchet potential, average motion due to flashing will be to the right. If the microsphere was started at minimum 1 (as defined in figure 5.4a) then it would have no possibility to move to the left. Even a symmetric ratchet would show a small average motion to the right in this case. For this reason we allow backstepping by starting the microsphere in potential minimum 3. Once the experiment is begun, the position is tracked in real time and one of the flashing algorithms is applied. The data collection continues until the bead reaches minimum 1 or 10. At this point data collection is paused and the bead is moved back to minimum 3, where the experiment can resume. This process was repeated until approximately 2×10^5 data points were collected, corresponding to a typical total displacement of more than 400 L.

There are three main topics discussed in this results section. First is a comparison between the optimal periodic flashing ratchet and a feedback controlled ratchet for $N = 1$. For the case of $N = 1$ the MIV and MND methods are equivalent. We then compare this result to Langevin simulations (simulations courtesy of Nathan Kuwada). Last, the performance of the MIV and MND methods are compared for $N = 1, 2, 3$ and $V_0 = 10\ kT, 30\ kT$, and $40\ kT$.

One important aspect of Brownian ratchets is that there must be no overall tilt to the potential. This is described in more detail in chapter III. To put it another way there should be no overall force. For our flashing ratchet system if we measure a particular magnitude of $\langle v \rangle$ to the right when the ratchet is as in figure 5.1, then we should measure the same magnitude of $\langle v \rangle$ to the left when the ratchet is mirrored.

Figure 5.5 shows a sample trajectory obtained by periodically flashing the ratchet near its experimentally determined optimal period of 700 ms, resulting in a time-averaged mean velocity of $\langle v \rangle = 0.068 \pm 0.01$ μm/s. Using the previously mentioned mirrored potential which gives average motion in the opposite direction we find $\langle v \rangle = -0.074 \pm 0.01$ μm/s, establishing a small negative bias of less than 10 nm/s that is within the experimental error.

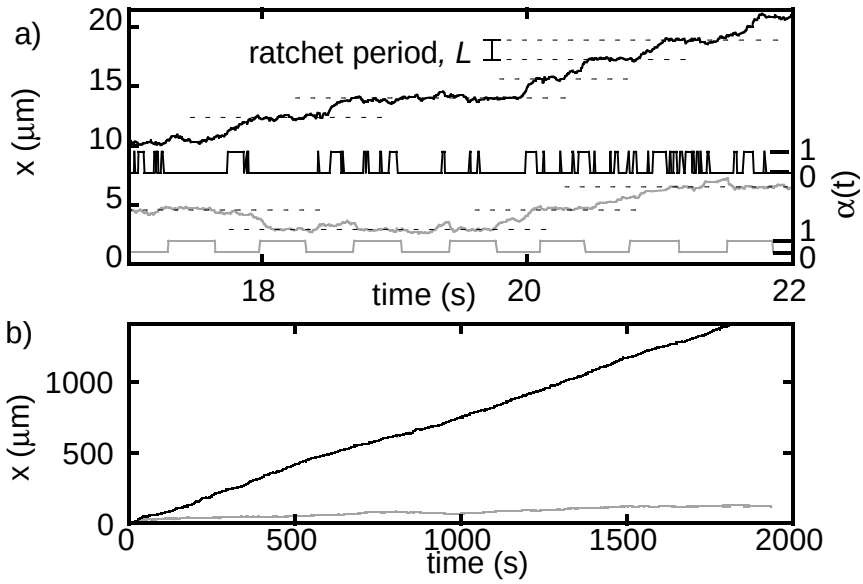

Figure 5.5. (a) Top black: particle trajectory for feedback-controlled ratcheting. Bottom black: $\alpha(t)$ for feedback trajectory. Gray: particle trajectory and $\alpha(t)$ for periodic ratcheting. (b) Longer time series of the same trajectories, generated by stitching together shorter runs.

The first presented result of feedback control is for $N = 1$. For this experiment $V_0 = 10$ kT (this is the measured potential in figure 5.4). In the case of $N = 1$ the MIV and MND algorithms are the same when $x_0 = 0$. We do not *a priori* know the optimal choice for x_0, so this value was varied and figure 5.6 shows the $\langle v \rangle$ obtained

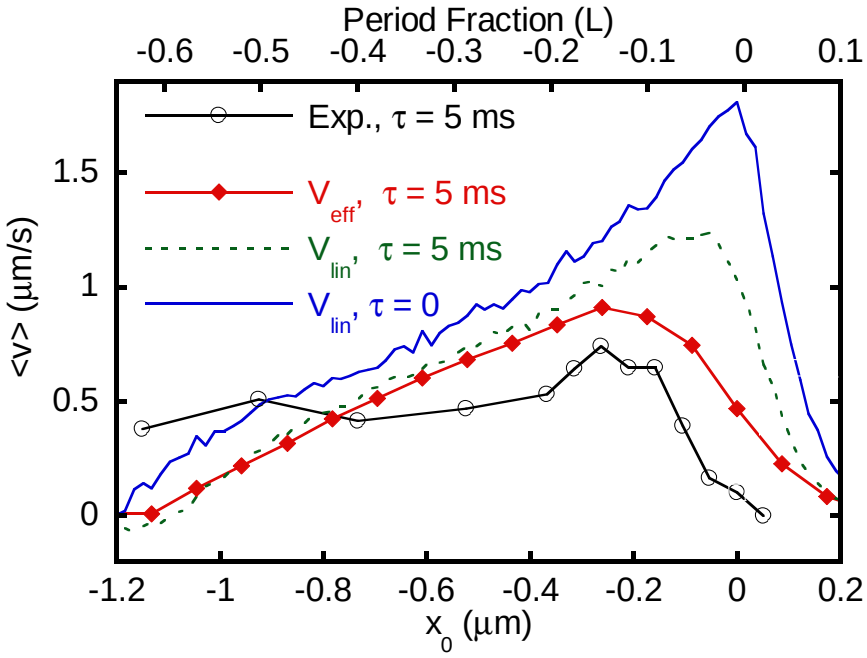

Figure 5.6. Average velocity $\langle v \rangle$ as a function of x_0 for $N = 1$ and MND. From the top: Simulated data using V_{lin}, $a = 0.33$, $\tau = 0$ (solid blue curve); V_{lin}, $a = 0.33$, $\tau = 5$ ms (dashed green curve); V_{eff} and $\tau = 5$ ms (red diamonds); and experimental data $\tau = 5$ ms (open black circles).

using the MND feedback algorithm as a function of x_0. We find a maximum $\langle v \rangle$ of 0.7 μm/s. This is the order of magnitude increase compared to the optimal periodic flashing ratchet, that had been predicted [49, 51].

The value of x_0 that gave the peak velocity as mentioned in the previous paragraph is $x_0 \approx -0.3$ μm, 0.15 L to the left of the minimum. Two factors that may affect this shift are the experimental feedback implementation delay, τ, and the effective potential shape. To better understand the roles of these two factors, we performed simulations as follows [51]. Particle trajectories were calculated by the overdamped

Langevin equation

$$\gamma \dot{x_i} = \alpha(t) F(x_i(t)) + \xi_i(t) \tag{V.11}$$

where $\xi_i(t)$ is a random number chosen from a Gaussian white noise distribution that has zero mean and correlation $\langle \xi_i(t)\xi_j(t')\rangle = 2\gamma kT\delta_{ij}\delta(t-t')$, and the external force is $F(x) = -\nabla V(x)$. Using for $V(x)$ the piecewise linear potential $V_{\text{lin}}(x)$ with $a = 0.33$ and no feedback delay ($\tau = 0$), the simulations predict a maximum ratchet velocity for $x_0 = 0$ (figure 5.6), where $x_0 = 0$ is always taken at the potential minimum. To include a feedback delay τ in the simulations, $\alpha(t)$ in equation V.11 is replaced by an effective delayed value, $\alpha(t-\tau)$. For $\tau = 5$ ms (equal to the experimental value), the simulations produce a somewhat reduced peak velocity at $x_0 \approx -0.1$ μm for the piecewise linear potential (figure 5.6). When using the same time delay and $V_{\text{eff}}(x)$ (equation V.10), we find that the peak velocity is shifted even further to negative x_0, to approximately the same position as in the experiment. Overall, we see a shift of x_0 to the left as the simulations become more similar to the experiment. This also holds for the declining peak $\langle v\rangle$ value. Including both V_{eff} and $\tau = 5$ ms in the simulations results in a close fit for the value of x_0 and $\langle v\rangle$. The simulation is not a perfect match to experiment, but there are certainly differences between the two that are not being taken into account.

From the experiment and simulations described we've shown that a nonzero τ introduces a shift of the maximum $\langle v\rangle$ to negative x_0 values. Why might this be? When there is no implementation delay, $\tau = 0$, once the microsphere reaches the

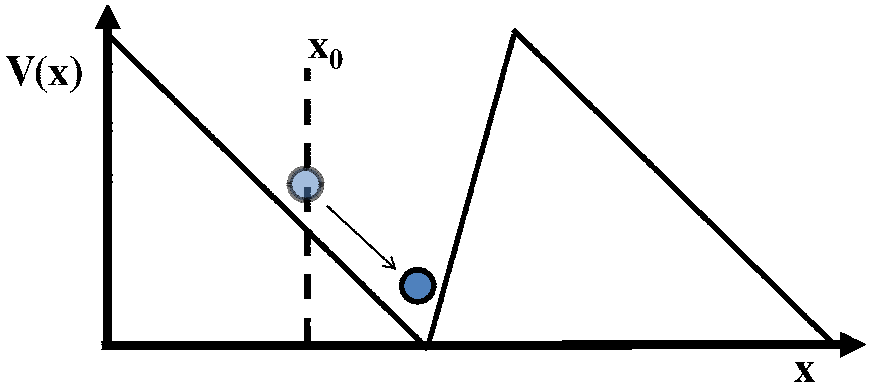

Figure 5.7. If the particle on average has a particular velocity, v, down the potential, and there is a feedback delay time, τ, then it makes sense to tell the algorithm to switch the potential at position $x_0 = -v\tau$ so that the particle is at the ratchet minimum when the potential really does switch.

bottom of the ratchet potential (and $x_0 = 0$) the potential shape can immediately change to flat and allow the opportunity for diffusion to work. However, if $\tau \neq 0$, then (again with $x_0 = 0$) the microsphere will reach the bottom of the ratchet potential and then wait τ seconds before it switches to the flat potential. Therefore, it is advantageous to anticipate the arrival of the microsphere by setting x_0 to the position that the microsphere will be τ seconds before it reaches a ratchet potential minimum (see figure 5.7). To test this explanation, figure 5.8 shows the x_0 that produces maximal $\langle v \rangle$ as a function of τ from simulations using $V_{\text{lin}}(x)$ with $a = 0.33$. Also shown are the distance $x_0 = -F\tau/\gamma$ a particle on the long slope would drift during τ due to the force of the ratchet potential, and the average distance $x_0 = \sqrt{2D\tau}$ a particle would diffuse during τ. For short τ, transport is actually primarily diffusive. The optimal choice of x_0 is indeed closely approximated by the diffusive prediction.

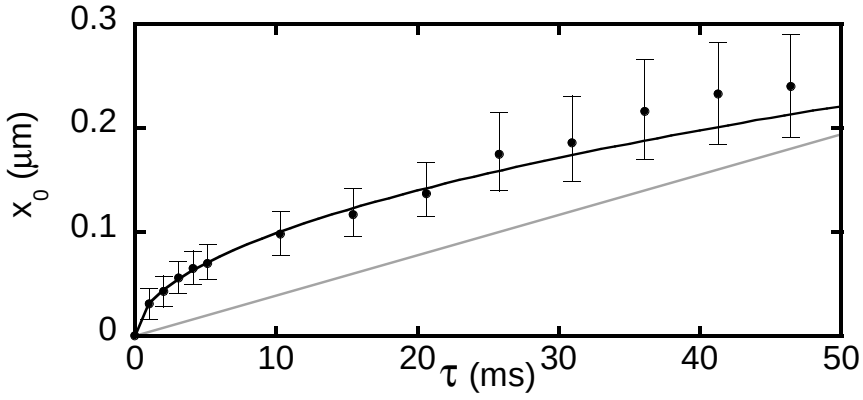

Figure 5.8. x_0 positions (circles) giving maximum $\langle v \rangle$ from curves such as the inset of figure 5.9 for various τ. For small τ these points fit well to a diffusive curve ($x = \sqrt{2D\tau}$, black line). Gray line: $x = -F\tau/\gamma$.

Figure 5.9 shows a comparison between using the spatial trigger x_0 (by finding the value that gives the maximum $\langle v \rangle$) or not using it (by setting $x_0 = 0$) for the case of $N = 1$. The lower curve shows the data reported in the seminal papers [48, 52] for the MIV scheme (equivalent to the MND scheme for $x_0 = 0$). The upper curve shows the optimal $\langle v \rangle$ found by simulating the MND scheme and varying x_0, demonstrating a substantial improvement for finite τ. The inset of figure 5.6 shows the simulated curve for each value of τ that was used to find the maximum $\langle v \rangle$.

For small $N > 1$ it has been predicted that the MND scheme can yield a moderately higher $\langle v \rangle$ than the MIV scheme [51]. To test this prediction, we performed experiments for $N = 2, 3$. To avoid any effects from particle-particle interactions, data points recorded when more than one bead was within any given ratchet period were excluded. For $N > 3$ this happens so frequently that sufficient data cannot be collected. In figure 5.10(a) we show experimental results for the ratio of average velocities obtained using

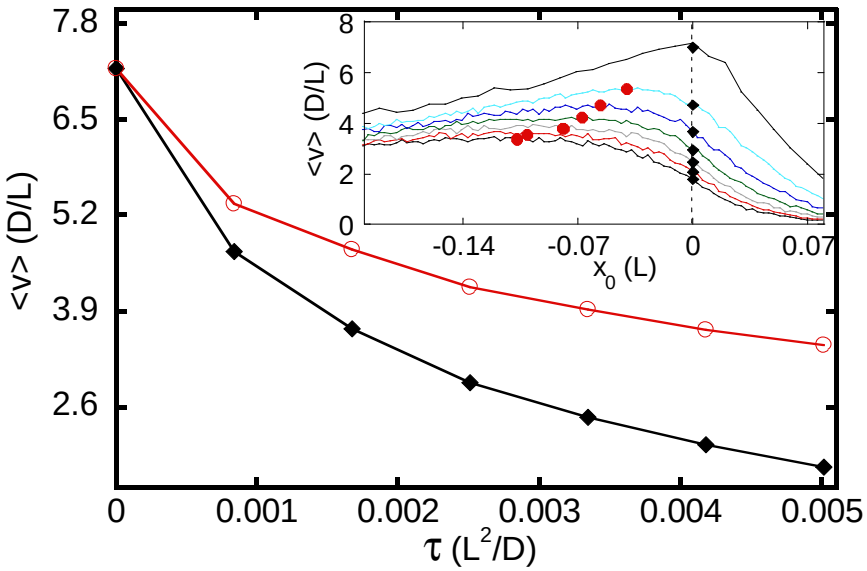

Figure 5.9. Simulated data using V_{lin} and $a = 0.33$. Black diamonds are from the MIV and MND scheme for $x_0 = 0$. Open red circles are the maximum $\langle v \rangle$ obtained using MND and by tuning x_0 for each value of τ. Inset: $\langle v \rangle$ as a function of x_0 for $\tau = 0$ to 0.005 L^2/D (top to bottom)

the two schemes. In each case, x_0 was varied, and the maximum $\langle v \rangle$ was used in figure 5.10(a). In agreement with simulations (figure 5.10(b)) that used $V_{\text{lin}}(x)$ with $a = 0.33$, $\tau = 0$ and optimal x_0 for MND, the MND scheme performs better than the MIV scheme for $N = 3$ and $V_0 \geq 30kT$. A difference not shown here is that in the simulation $\langle v \rangle$ increases with V_0 in all cases, whereas in the experiment we see an unexplained overall drop between $V_0 = 30kT$ and $40kT$. This may be due distortions in $V(x)$ at high V_0.

We have demonstrated diffusive particle motion in customized, time dependent potentials with fast feedback. This was the first system to experimentally test the predictions of $\langle v \rangle$ increases due to feedback control. The order of magnitude increase

in feedback compared to optimal periodic flashing was shown. The spatial trigger x_0 was demonstrated to provide moderate increases in $\langle v \rangle$ for nonzero feedback implementation delay. Good agreement between the experiment and simulations were found when both feedback implementation delay and the effective potential ratchet shape were taken into account in the simulation. In the future this system could also be used to realize sorting devices akin to Maxwell's demon, or to study particle-particle interactions in ratchets.

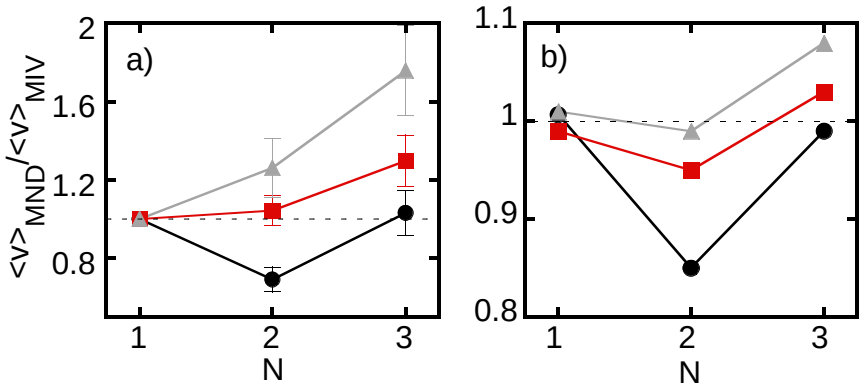

Figure 5.10. Ratio of $\langle v \rangle$ obtained for MND and MIV methods for various N and $V_0 = 10kT, 30kT, 40kT$ from bottom to top. (a) Experimental data for optimal x_0. (b) Simulated data using V_{lin}, $a = 0.33$, $\tau = 0$ and optimal x_0 for MND.

CHAPTER VI

MOLECULAR MOTORS

Biological cells are complex systems consisting of many parts and processes. Some of these processes are performed by cellular components that convert chemical energy into mechanical energy or vice-versa. These components are referred to as molecular motors. This chapter gives background information about molecular motors designed to show their importance to the cell and the interest in them from the biophysical community. Examples of several molecular motors are given and some of the research that has been done. After this the interest in artificial molecular motors is described, as well as the work of our research group and collaborators in this regard. Specifically, we are designing and constructing artificial molecular motors, the tumbleweed and the inchworm. We are motivated to pursue the single-molecule assay described in chapter VII as a way to understand and predict the behavior of those motors.

Biological molecular motors are proteins. A protein is a chain of amino acids and its function is determined by its structure. There are 22 standard amino acids. Amino acids are differentiated by the chemical makeup and structure of their side chains. (See figure 6.1 for chemical structure diagram.) One key property of the side chains is their hydrophobicity. Hydrophobic side chains are in a lower energy state when they interact with each other rather than water, and hydrophillic side chains are in a

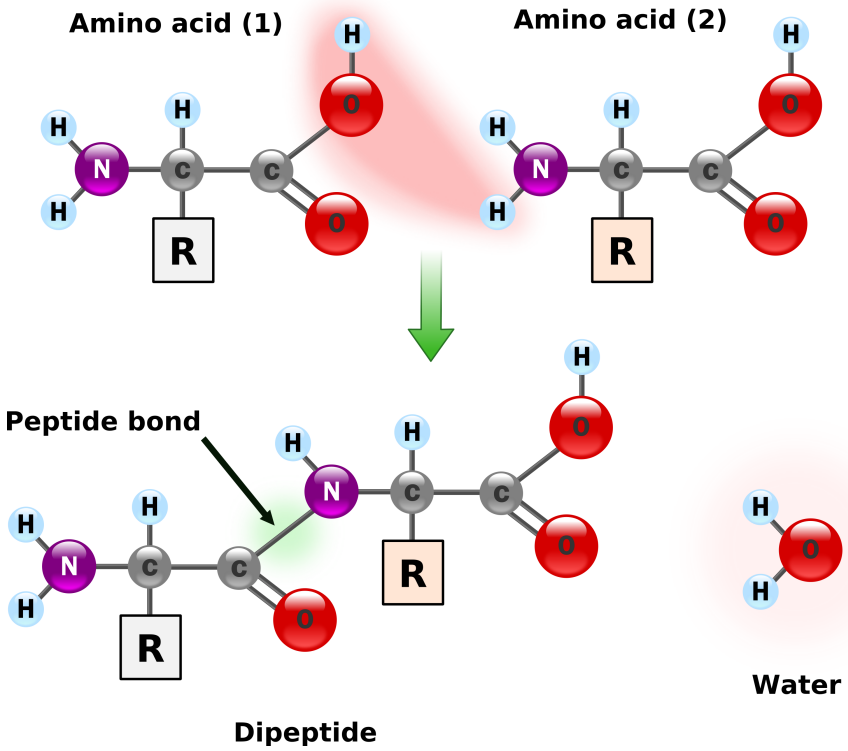

Figure 6.1. Diagram of the reaction between two amino acids that forms a peptide bond necessary to make long peptide chains. R is the location of the side chain. The makeup of the side chain determines which amino acid it is. Public domain image from http://en.wikipedia.org/wiki/Amino_acid.

lower energy state when they interact with water. When a protein is synthesized in a cell it starts as a long chain of amino acids, and because of its specific sequence of amino acids, it folds into a particular shape that gives a low energy state. One of the ways this is achieved is by hiding hydrophobic side-chains within the structure of the protein and exposing hydrophillic side-chains. There are other factors such as steric effects, hydrogen bonds, and disulfide bonds that contribute in determining the final structure of a protein [56].

One example of a biological molecular motor is F_0F_1 ATP synthase (figure 6.2). ATP, adenosine tri-phosphate, is the primary energy molecule of the cell. It is produced by an energy-requiring chemical reaction between ADP and inorganic phosphate (P_i). The F_0 portion resides in the mitochondrial membrane and the F_1 portion is in the mitochondrial matrix. In normal operation in the cell, ATP synthase catalyzes the reaction of ADP and P_i using the energy of moving protons from the proton-rich side of the membrane to the proton-poor side. This imbalance of protons is created by the electron transport chain, a series of reduction-oxidation reactions involving metabolic intermediates. The proton gradient causes a rotation in the F_0 domain which opens and closes ADP and P_i binding pockets in the F_1 domain. ATP synthase is a rotational motor. It has been found in experiments [57] that forcefully rotating the F_1 domain in one direction resulted in ATP production and in the other direction resulted in ATP hydrolysis.

Linear Molecular Motors

The Tumbleweed and Inchworm motors are most similar to a class of biological molecular motors referred to as linear motors. Linear motors travel unidirectionally along tracks in the cell; the type of track depends on the motor. There are three classes of linear motors in the cell: myosins, kinesins, and dyneins. There are dozens of each of these motors. Myosins walk on actin filaments and kinesins and dyneins walk in opposite directions on microtubules. They all have dimeric forms, meaning that they

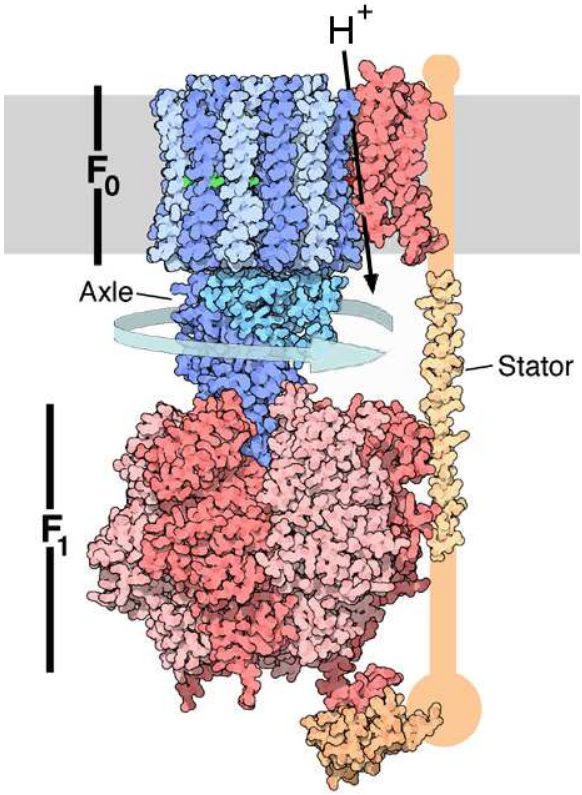

Figure 6.2. Protein structure of F_0F_1 ATP synthase from x-ray crystallography methods. The F_0 portion of the protein lies in a membrane. The proton gradient pushes protons from one side of the membrane to the other and this process turns the axle that lies within the F_1 portion of the protein. This catalyzes the reaction of ADP and inorganic phosphate into ATP. Image freely distributable under GNU Free Documentation license and was found at http://en.wikipedia.org/wiki/ATP_synthase.

are composed of two identical subunits which bind together. These dimeric, linear motors are composed of two heads that bind to their respective tracks. The heads are connected by a protein stalk. For myosin and kinesin there is an ATP binding site in each of the heads, and for dynein there is a binding site in the body of the protein. Each of these work by converting the chemical energy of ATP hydrolysis into a conformational change of the protein that is amplified into significant mechanical change by the structure of the protein [58]. These linear motors have two separate heads that hydrolyze ATP. The head's interaction with ATP can be in several different states: bound, unbound, or bound as ADP (ATP that has lost one phosphate group after hydrolysis). The state that the head is in determines its ability to bind to the track. If each head went through its chemical cycle entirely independently, the motors wouldn't have the high processivity that is observed. Both heads would become unbound to the track at the same time, much more frequently. Because of this, there must be some coordination between the chemical cycles of each head. This is referred to as gating. The most common mechanism used to explain gating is intramolecular strain [33, 59, 60]. The two heads are connected to each other by the rest of the protein. When both heads are bound, the chemical state of each head can be communicated to the other through strain in the molecule.

Kinesin (figure 6.3) takes 8 nm steps that occur in microseconds. While ATP is bound to the foot that is attached to the microtubule the other foot undergoes a biased diffusion to find the next binding site. It has a stall force of about 7 pN

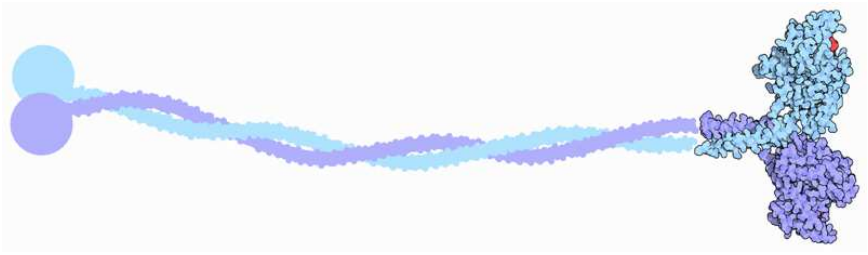

Figure 6.3. Structural image shows a dimeric kinesin protein (black outline) with attached linker (no outline). Kinesin attaches to microtubules with its two heads (rightmost side of the figure). Public domain image from http://en.wikipedia.org/wiki/Kinesin.

and at larger forces will undergo backstepping with dwell times that are dependent on ATP concentration [32]. When exerting a force on a molecular motor (possibly using an optical trap as described in chapter IV), the stall force is the force at which the molecular motor will make neither forward nor backward steps, on average. The chemical cycles of the two feet are gated with respect to each other and this allows a near perfect 1:1 ratio of ATP per step. This gating is almost certainly due to mechanical strain within the molecule [33].

Myosin-V (figure 6.4) is one of the more studied in the myosin family of proteins because of its relatively large, 36 nm, step size. Like kinesin it consists of two feet connected by a stalk, and it hydrolyzes ATP in its stepping process. Myosin is a weaker motor than kinesin since it has a stall force of only 2 pN [34, 35]. This may be surprising since it has the same amount of free energy per ATP hydrolysis available for stepping. The energy of ATP hydrolysis is used to do work. For a molecular motor that is stepping against a force, F, and takes steps of size Δx, the work done is simply defined as $W = F\Delta x$. Given the same energy available to do work, one expects an

inverse relationship between step size and stall force. Myosin takes larger steps than kinesin (36 nm to 8 nm respectively), and this may be what has allowed researchers to experimentally observe substeps. The first of these substeps is a few nanometers forward as the internal strain in the molecule is generated. Next there is a substep that happens after the rear foot detaches (about 25 nm). It is hypothesized that this happens because the internal strain relaxes, leaving the last few nm to be negotiated by diffusion [60, 61]. This model was found to work successfully in a detailed Langevin simulation with few free parameters [62]. In this simulation the myosin-V molecule was modeled as a chain of eight rigid segments with some flexibility between each of the segments. The motor feet had binding kinetics with values take from experiment and intramolecular strain was introduced depending on the kinetic state of those feet. Incorporating all of these aspects, with the correct diffusive behavior of the segments, provided a confirmation of the strain-induced gating hypothesis as well as replicating experimental values for speed and stall force. An additional aspect of these simulations is that animations were able to be made directly from the data. Visualization of this nature can help people to form an intuitive understanding of the motion of molecular motors.

Our Artificial Protein-based Molecular Motors

Since the function of a protein depends on its structure, building a protein-based molecular motors is a way to test our understanding of the structure-function

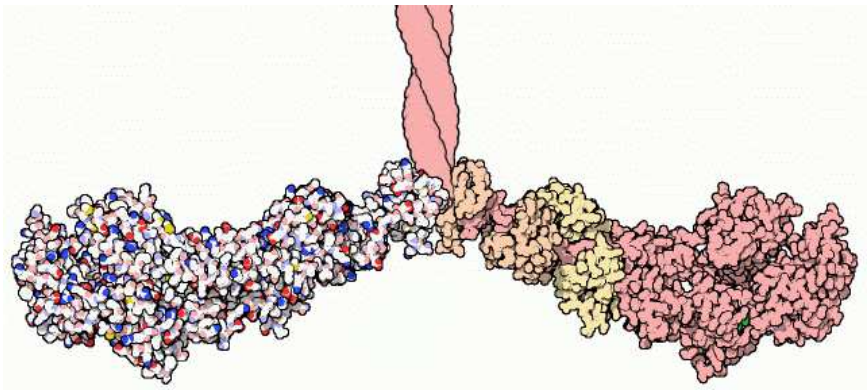

Figure 6.4. Structural image of myosin-V (detailed with black outline) with linker (undetailed, pink). Myosin binds actin, a structural material in the cell. In this orientation actin would bind to the heads of the protein at the bottom of the image. Image courtesy of David S. Goodsell of the Scripps Research Institute, with permission.

relationship. An intentional structural design forms a prediction of the function and single-molecule experiments of the final, constructed motor can be used to observe and test the function of the artificial molecular motor. Molecular motors have been studied for a while now, and the knowledge of their function has increased greatly. With regards to the famous Richard Feynman quote "What I cannot create, I do not understand" [63], there is a utility in attempting to design our own molecular motor. The process of design can be a test of our knowledge; it can expose gaps in our understanding. There are other efforts to make artificial molecular motors based on DNA [64–67], but our tumbleweed and inchworm motors are the only ones that are protein-based.

As part of an international collaboration, the Linke group is involved in the design and characterization of the tumbleweed motor [68]. The design of the Tumbleweed (TW) involves a central hub with three coiled-coil protein chains protruding radially,

with a different orthogonal DNA repressor protein at the end of each chain (see figure 6.5). These proteins are orthogonal in the sense that they bind to different DNA sequences and depend on different ligands to activate their binding. This molecular motor would take processive steps on a DNA track encoded with the correct, ordered binding sequences, and binding would be gated through timed insertion and removal of ligands into solution. Steps would be on the order of tens of nanometers. Protein design is currently not advanced enough yet to build ligand activated DNA binding subunits. For that requirement we use nonmotor proteins found in E. Coli. There are three proteins for the three feet of the TW, one for each foot. The proteins are TrpR, MetJ(Q44K), and DtxR. These proteins are DNA repressor proteins about 24 kDa in size in their dimer forms. They bind to a certain sequence of DNA in the presence of a ligand, since they are dimers the sequences that they bind to are palindromic. The ligand for TrpR is tryptophan. The ligand for MetJ is s-adenoysl methionine. The ligand for DtxR is iron or nickel. These proteins can be easily expressed in E. Coli using standard molecular biology techniques (see appendix A).

A second artificial molecular motor, the inchworm (IW), is also being developed. In this design the geometry is inverted compared to the TW, and a carpet of two repressor proteins become the track and the DNA with one of the protein binding sequences at each end acts as the motor. When DNA is introduced into small nanochannels (100 nm width), its conformation changes from globular to elongated. The extension of the DNA doubles as the ionic strength of the solution is decreased by

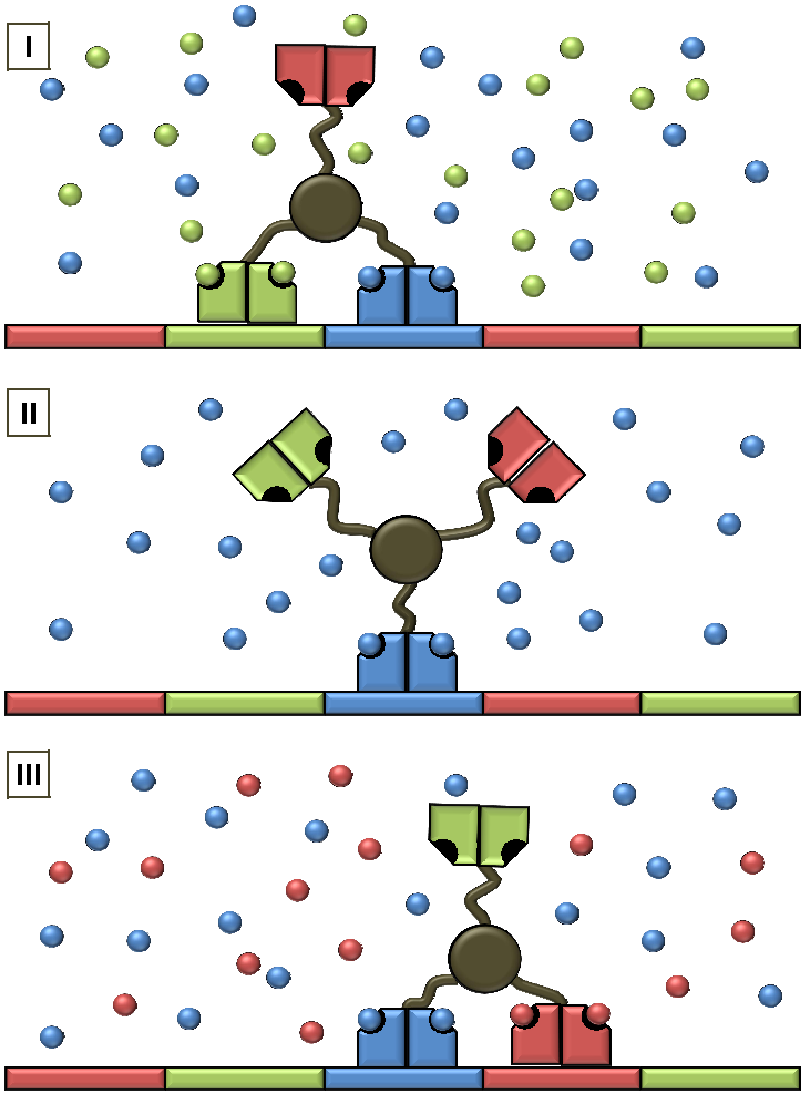

Figure 6.5. (Green=G, Red=R, Blue=B.) The tumbleweed motor cycle: I) With ligands G and B present in solution, dimeric DNA binding repressors G and B bind to the corresponding portions of the DNA track. II) Ligand G is removed from solution and repressor G dissociates from the track. III) Ligand R is introduced into solution and repressor R diffuses until it reaches binding site R and binds. With the cycle continuing in this manner, processive motion will occur.

two orders of magnitude [69]. By carefully coupling this large conformational change of the DNA to binding proteins at either end, micron scale steps could be observed. In contrast to the TW, the IW uses binding to rectify large conformational shifts (see figure 6.6).

Both of the proposed artificial molecular motors, IW and TW, require controlled switching of ligands in solution to achieve motion. This would happen in a certain period of time, T_{lig}. There are two important timescales involved with these proteins. τ_{off} is the time scale for dissociation of the DNA-protein complex without the presence of the ligand, and τ^*_{off} is the time scale for dissociation of the same in the presence of the ligand. Both of these are the inverse of their related rate constant. It is important that the time for the controlled switching of ligands falls between these two timescales:

$$\tau^*_{\text{off}} > T_{\text{lig}} > \tau_{\text{off}}. \tag{VI.1}$$

An original method has been developed to measure τ^*_{off} and τ_{off} and is explained thoroughly in the next chapter.

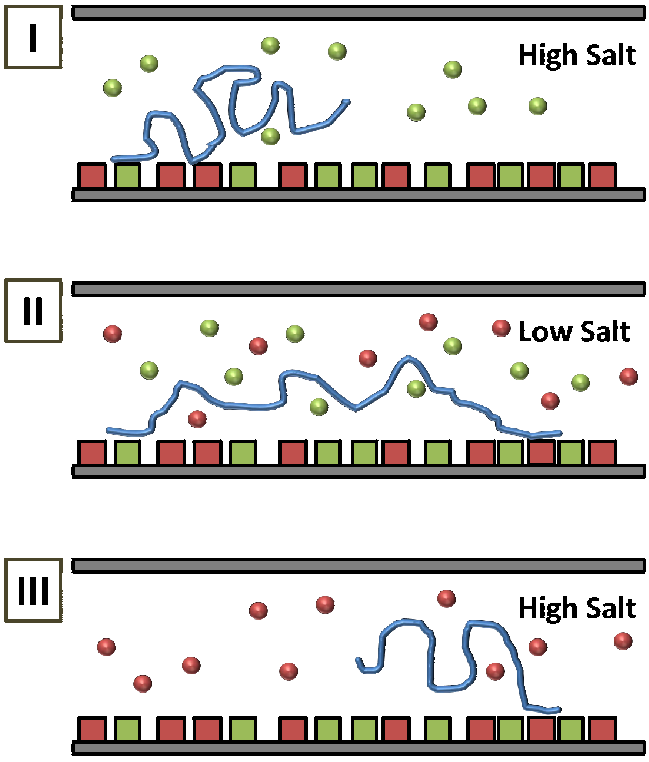

Figure 6.6. (Green=G, Red=R) The DNA molecule is represented by the blue curve. Its left end has the binding sequence for protein G and the right end has the binding sequence for protein R. The Inchworm motor cycle: I) With ligand G present in a high salt solution, the DNA molecule binds to repressor protein G at one end and the other end doesn't bind. II) In a low salt solution the DNA molecule extends and when both ligands are present in solution both ends of the DNA bind to one of the proteins. III) Ligand G is taken out of solution and the DNA molecule unbinds from protein G. Then when a high salt concentration is introduced the DNA molecule's length reduces. There is net center of mass motion in this cycle.

CHAPTER VII

PARALLEL SINGLE-MOLCULE BINDING KINETICS

In an attempt to understand and anticipate the behavior of the tumbleweed and inchworm motors it is useful to know the binding and unbinding rates ($k_{\text{on}}, k_{\text{off}}$) of the repressor proteins (TrpR, MetJ, and DtxR) that are key components of both of these motors. Since we intend to observe these motors at a single-molecule level, it would be useful to understand the repressor proteins at a single-molecule level also. With this motivation a single-molecule technique using much of the same setup and tracking system as the feedback ratchet experiment was devised.

This chapter begins with a description of the proposed single-molecule experiment and a rationale for why a single-molecule unbinding rate experiment is important. Before doing the single-molecule experiment it was necessary to find a method to immobilize the repressor proteins on a surface since the single-molecule assay design requires this. The next section discusses the bulk assays used to establish the surface immobilization method and to qualitatively establish the protein activity. Once the immobilization method was tested and decided upon, the actual single-molecule experiment was begun. The original plan was to collect enough single-molecule data to establish reliable values for the unbinding rates of the repressor proteins involved in the TW and IW motors . Unfortunately, due to time constraints what

has been established is the effectiveness of the method via several controls which are discussed thoroughly in the single-molecule experiment section. Using artificial diffusive-tethered-diffusive single molecule trajectories, the accuracy of this assay to measure unbinding times was found. Finally the chapter finishes with a discussion of the feasibility of the experimental method and what potential applications it could have.

Description of the Proposed Single-molecule Experiment

Our single-molecule assay is a variation of a tethered particle motion (TPM) experiment. TPM assays use the Brownian motion of an observable particle to determine information about a coupled molecule that is not as easily observed. The most typical configuration of a TPM assay uses a hundred nanometer to several micrometer bead that is connected to one end of a single DNA molecule. The other end of the DNA is fixed to a surface. A protein is in solution that has the ability to bind to multiple sites on the DNA strand at the same time. When multiple sites are bound, the DNA is looped and its end to end distance is reduced (see figure 7.1). By observing the diffusive motion of the bead, it can be determined if the DNA is looped or not. One use of TPM was observing the binding behavior of the LacI repressor [70]. This experiment used 1151 base pair DNA with Lac operator sites separated by 305 basepairs. TPM assays have also been used to study transcription by RNA

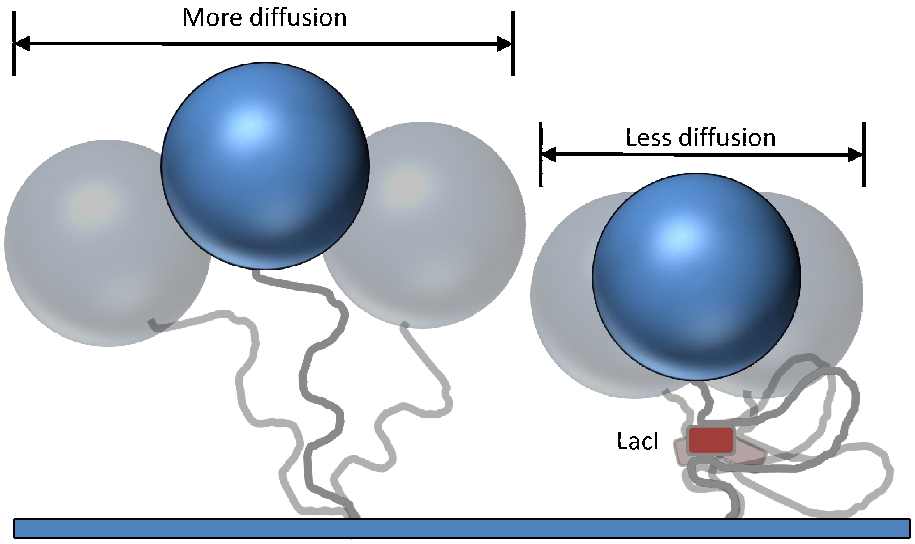

Figure 7.1. In a TPM assay, the tether length changes when a protein (such as LacI) binds two regions on the DNA creating a loop. This can be observed by noticing the reduced diffusion of the microsphere because of the looped DNA versus the unlooped DNA.

polymerase [71, 72]. In these experiments the tether length changes smoothly instead of transitioning quickly between two lengths.

In our new method, like in a TPM assay, the diffusive motion of a microsphere is used to determine the chemical state of a DNA binding protein. Unlike TPM the state of the protein is changing from unbound to bound and the diffusion of the bead changes from free diffusion to tethered diffusion (see figure 7.2). This is in contrast to standard TPM where the length of the tether is changing due to a DNA looping protein. This variation of the TPM method extends it to use with one-site binding DNA repressor proteins, such as those used as components in the TW and IW motors. This assay would measure the distribution of unbinding times of the repressors. By

fitting an exponential function to that distribution, one would find the unbinding rate, k_{off}. It is also possible that an exponential function will not fit well to the distribution. This is a possibility because we are measuring at a single-molecule level and would be an interesting result. For the repressors planned to be used in the TW and IW motors there have been experimental measurements of K_d [73–75]. For a simple two-state process such as

$$\text{DNA-repressor complex} \rightleftharpoons \text{DNA} + \text{Repressor}, \tag{VII.1}$$

K_d is defined as the ratio of concentrations at equilibrium:

$$K_d = \frac{[\text{DNA}][\text{Repressor}]}{[\text{DNA-repressor complex}]}. \tag{VII.2}$$

If both K_d and k_{off} are known then we can find the binding rate k_{on} using this relationship:

$$K_d = \frac{k_{\text{off}}}{k_{\text{on}}}. \tag{VII.3}$$

There are advantages to single-molecule (SM) experiments compared to traditional bulk measurements. Bulk measurements sample the average value from a very large population of molecules. This population may be heterogeneous in activity or behavior. A SM assay could potentially identify two separate populations of molecules [76]. An experimental difficulty of a bulk kinetic measurement is the necessity of switching or mixing solutions quickly on the scale of the reaction. Any measurement of this nature must account for that time at nonequilibrium. SM measurements can be done at equilibrium since the stochastic kinetic process of binding and unbinding can be

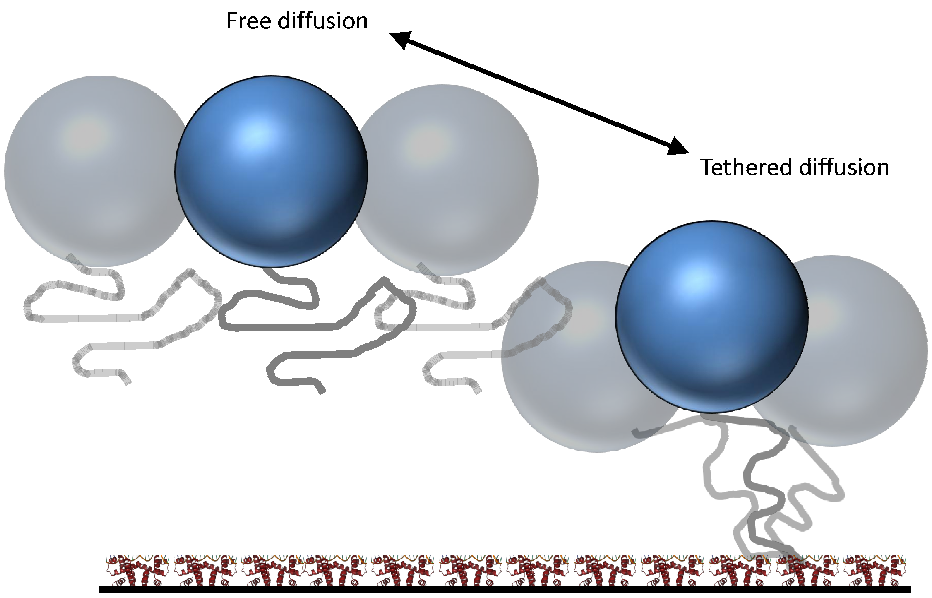

Figure 7.2. In our single-molecule assay, we track the change between free diffusion to tethered diffusion and vice versa. This enables us to use a simple method similar to TPM assays, but expands its use to proteins that only bind one sequence of DNA. The details of the immobilization method are shown in a later figure.

directly observed instead of inferred from ensemble rates. Specifically for the TW and IW projects, since these motors will function and be observed at a single molecule level, doing these experiments in a similar way is reasonable.

Bulk Surface Binding Assays

Before doing single-molecule experiments with the DNA repressors, it was necessary to test both the surface functionalization and the qualitative binding activity of the repressors. The functionalization is needed to immobilize the proteins on a surface for both the single-molecule assay and for the experimental design of the inchworm. Functionalization of the surface is intended to reduce non-specific binding

of the repressors and introduce a specific binding that does not interfere with protein activity. Both our single-molecule assay and the IW motor experiment will need to be functional for a minimum of one hour. The immobilization of the proteins needs to have a lifetime of at least this length.

In general proteins will adsorb to a glass surface and at least partially denature in the process. A protein is held together in great part by the hydrophobic or hydrophilic nature of the side chains of its amino acids. Once a protein is on a surface and not entirely surrounded by water this sensitive balance can be disturbed and denaturation or loss of function can occur. It is possible that a protein may function in this situation, but there are several reasons it may not. One, the binding site of the protein may be occluded by the glass surface. Two, the denaturation of the protein could destroy or change the activity of the binding site. Also, in the case of the ligand gated repressor proteins used in the IW and TW, both the ligand and DNA binding sites might have these problems.

As an aside, the genetic sequences that code for the proteins used in these experiments were modified to code for a his-tag at the c-terminus (carboxyl end) of the amino acid chain. This tag is made up of a linker of several glycines (amino acids with a very small side chain) and then six histidines. The histidines will bind cooperatively to a nickel nitrilotriacetic acid (NiNTA) group. The his-tag was added to the protein to facilitate protein purification (see appendix A). This was done by our collaborator

Dr. Roberta Donadini at University of New South Wales. Our first idea was to also use this as a handle for surface immobilization.

We investigated two different methods for surface functionalization. The first method we tried involved using a gel-phase lipid bilayer with NiNTA labeled lipids to bind to the his-tags of the repressor proteins. Two different experiments were used to evaluate the performance of this method. First, we used a standard fluorescence microscope and measured an average brightness over a field of view to determine bilayer formation and to observe DNA binding to the surface. Because of bleaching effects and the inability to directly measure protein binding to the bilayer, we then did experiments using a quartz crystal microbalance device (which can measure unlabeled protein binding directly). The second functionalization method we tested was direct adsorption of neutravidin to the glass surface. We tested this method using a TIRF spectrophotometer.

Gel-phase lipid bilayer functionalization

The first surface functionalization tested was a gel-phase lipid bilayer. The lipid makeup of this bilayer is: 96% DPPC , 1% DGS-NTA, 3% PC-NBD. Due to the DPPC lipid, this mixture forms a gel-phase bilayer at room temperature and has a gel to liquid transition temperature of 40°C-43°C (Avanti Lipids). Bilayer formation has been verified in a microscope using FRAP (fluorescence recovery after photobleaching). The FRAP technique relies on bleaching the fluorescent markers on biomolecules within a spot, and then observing the time it takes for fluorescence in that spot to

recover due to new markers diffusing into the bleached area [77]. The DGS-NTA lipid has a modified headgroup that includes a NiNTA group which binds to the his-tag of the repressors. The PC-NBD lipid has a modified tail that includes the fluorescent molecule NBD. 1% DGS-NTA corresponds to one molecule in every 8-by-8 nanometer square. For molecules the size of the repressors, the above density is equivalent to 120 mg/ml protein concentration at 100% binding. With DNA bound 1:1, the DNA concentration is 100 mg/ml. These are very high concentrations.

The experimental protocol is written in detail in appendix A. A diagram of the functionalization scheme is shown in figure 7.3. Briefly, vesicles with the makeup described above are incubated in the prepared microchamber. In the microscope, bilayer formation is verified using FRAP. A solution containing protein is injected into the microchamber. The protein is given a few minutes to bind to the NiNTA labeled lipids. Then DNA with the correct ligand for the protein is injected in to test binding. Each dsDNA oligomer molecule (oligo) has the recognition site for the protein and is labeled at one 5' end with a Texas Red fluorophore. Using traditional fluorescence microscopy, the labeled oligos will be visible as a uniform brightness across the field of view. With ligand in solution, the oligos should bind to the repressor proteins on the surface of the microchamber. After injecting more solution with ligand but no DNA, there will be a localized fluorescence only near the surface of the chamber since free, unbound oligos will be washed away. If DNA with no ligand in solution is injected

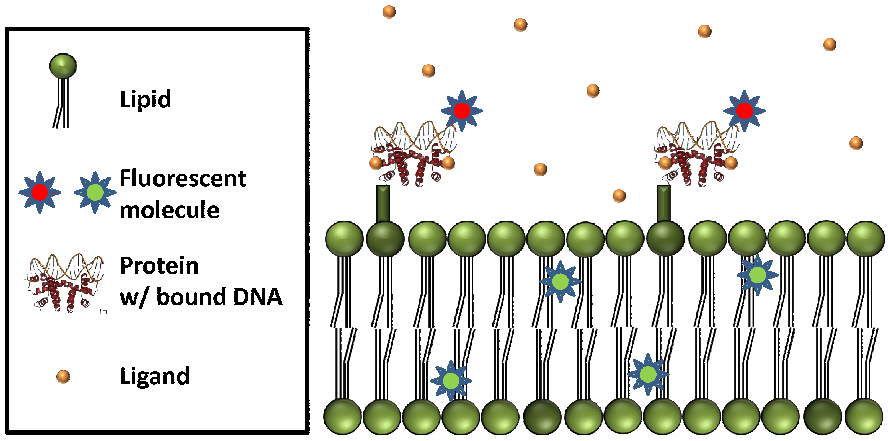

Figure 7.3. This diagram shows the surface functionalization scheme for the gel-phase lipid bilayer assay. First the lipid bilayer with fluorescent markers is formed and tested using FRAP. A repressor protein is introduced into solution and binds to the DGS-NTA lipids using the his-tag on each protein. Then DNA and ligand are introduced into solution. The DNA has a fluorescent marker of a different color than the lipid and can be observed independently. A weakness with this assay is that if the DNA fluorescence is not observed there can be two causes. Either the DNA did not bind to the protein, or the protein did not bind to the lipids. The results of this assay are shown in figure 7.4.

there should be a much smaller binding signal because protein-DNA affinity is much lower without the presence of ligand.

There are problems with this assay. There is a small, but resolvable difference between bound oligos and no oligos (red and green curves in figure 7.4). Unfortunately, there is significant bleaching each time an image is acquired. The small difference between red and green curve in figure 7.4 can be attributed to bleaching. We can't be certain that the difference in the two curves is due to a lack of DNA bound to protein in the green curve. Another potential issue is the protein unbinding from the

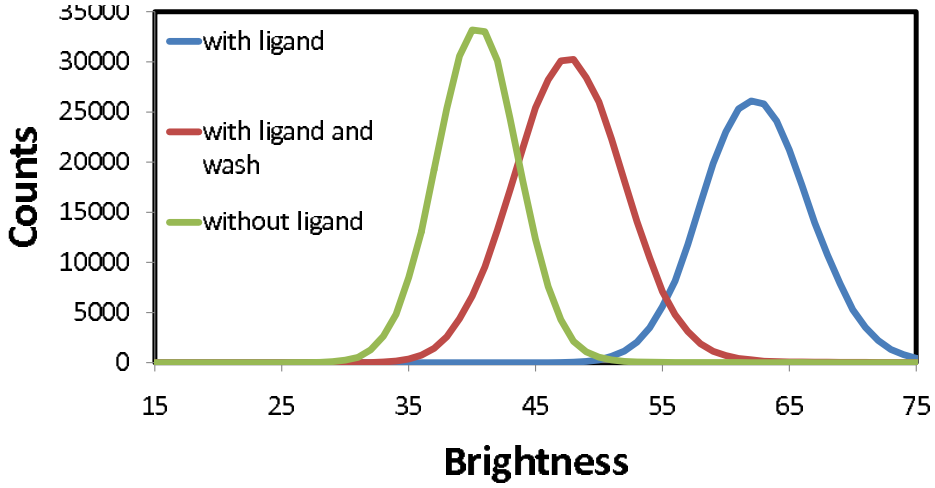

Figure 7.4. Brightness histogram of images taken from bulk fluorescence experiment with TrpR. Blue curve (right): histogram from image taken after introduction of labeled oligos into solution. Red curve (middle): histogram from image after flushing with binding buffer containing the ligand. This washes away unbound oligos and leave those bound to TrpR. Green curve (left): histogram from image after washing with binding buffer without ligand. The bound oligos unbind and wash away from the surface. The intensity is only due to background at this point.

NiNTA labeled lipids. As in many chemical reactions, this is an equilibrium process, and continued washing pushes the reaction towards unbinding.

With FRAP we have established that a gel-phase lipid bilayer does form. We can measure the fluorescence of the labeled DNA, but the assay bleaches quickly and we are unable to distinguish between controlled unbinding and bleaching. Since there is no fluorescent label on the protein, there is no direct measurement of protein binding to the NiNTA labeled lipids. A method is needed to directly measure protein binding to the functionalized surface. A QCM device can be used to directly measure unlabeled protein binding to a surface.

A quartz crystal microbalance (QCM) is a piezoelectric device. An oscillating

electric field applied across the device creates an acoustic wave. It operates in shear mode, that is the acoustic wave travels perpendicular to the surface of the device [78]. The change in resonance frequency that a QCM operates at is proportional to the change in the mass of the device [79]:

$$\Delta F = -\frac{2F_0^2}{A\sqrt{\mu_Q \rho_Q}} \cdot \Delta m. \tag{VII.4}$$

In this equation F_0 is the fundamental frequency of the device, A is the surface area, μ_Q is the shear modulus and ρ_Q is the density of the quartz. Δm is the change in mass. Because of this relationship a change in mass of the device can be measured as a shift in the resonant frequency. Surface layer deposition onto the QCM device can be measured in real time by the shift in resonant frequency. Since a QCM measures the mass attached to a surface directly (without the need for a fluorescent label), this device can measure the protein binding to the lipid separately from the DNA binding to the protein. A QCM setup was used to observe the formation of the surface layers.

QCM experiments (figure 7.5) show that the histag-NiNTA binding isn't as strong as required. As mentioned before, the binding of his-tag to the NiNTA is an equilibrium reaction, so when there is no his-tag proteins in solution, there will be a net loss of bound protein. This happens too quickly for our single molecule experiments (50% loss of bound protein within 20 minutes), and is also a poor solution for the IW project.

Neutravidin adsorption functionalization

Since the NiNTA and his-tag surface immobilization method didn't provide binding

that was stable over the length of time necessary for the single-molecule experiment or for the IW motor, we tested a second method. This method uses direct adsorption of neutravidin (NA), a modified version of streptavidin, to the glass surface of a coverslip. Streptavidin is a naturally occurring protein that is capable of binding four biotin molecules with a very high binding affinity. It is commonly used in biotechnology applications since it is one of the highest affinity, non-covalent, binding events known [80]. NA has been modified by mutating some charged amino acids to neutral amino acids. The mutations reduce nonspecific binding while maintaining the same binding characteristics [81]. The repressor protein can be chemically modified to have a few biotin molecules on it. If the NA adsorbs to the surface and retains its biotin binding activity, then biotinylated repressor protein will bind to the NA.

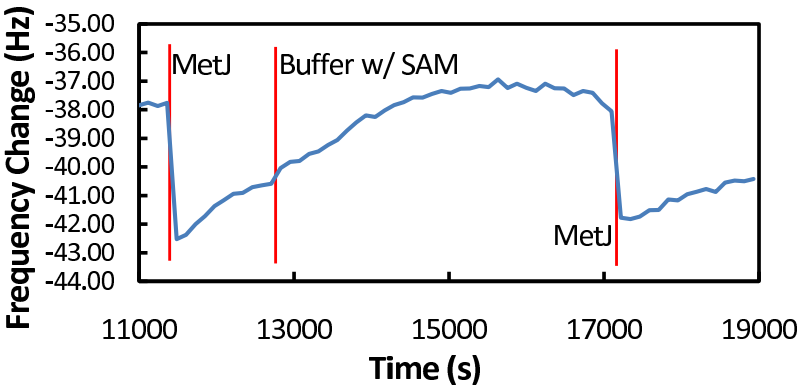

Figure 7.5. At the beginning of the plot a lipid bilayer containing a percentage of NTA labeled lipids has been established. The first red line marks the introduction of MetJ into solution and shows the protein binding to the lipid bilayer by a 5 Hz frequency change. Immediately MetJ begins releasing from the surface and this problem is exacerbated by the wash of HEPES buffer containing the ligand SAM (second red line). At the third red line MetJ is again brought into solution and rebinds to the surface and starts dissociation like before.

This immobilization method was tested using a TIRF spectrophotometer device. TIRF (total internal reflection fluorescence) is an illumination technique that uses the evanescent waves from total internal reflection as the excitation light for fluorescent molecules. These evanescent waves extend only about 100 nm into the sample and are used to excite only fluorescent molecules near the surface of the chamber [82]. This reduces the background noise of fluorescent molecules far from the surface.

In figure 7.6, it can be seen that NA at 100 μg/mL with 10% of the NA fluorescently labeled adsorbs to the surface of the chamber. It stays adsorbed to the surface after the NA is removed from solution. From the discussion a few paragraphs earlier, we know that the function of a protein may be affected by denaturing on the surface that it is adsorbed to. A measurement of the binding of biotinylated TrpR to the surface adsorbed NA was done (figure 7.7). A TIRF spectrophotometer is sensitive enough to measure the inherent fluorescence of a protein without a fluorescent label. The inherent fluorescence of TrpR quickly bleaches, but there is still a measurable binding curve. Figure 7.8 shows the binding of operator DNA, with and without ligand present, to the bound TrpR. With ligand, the DNA binds and stays bound until washed away with solution without ligand or DNA. The curve follows the characteristic shape of a binding curve, $1 - e^{-t/\tau}$. Without ligand, there is no binding curve. It resembles a step function. This is likely to be the result of unbound DNA close enough to the surface to be excited by the TIRF illumination. It is a background signal.

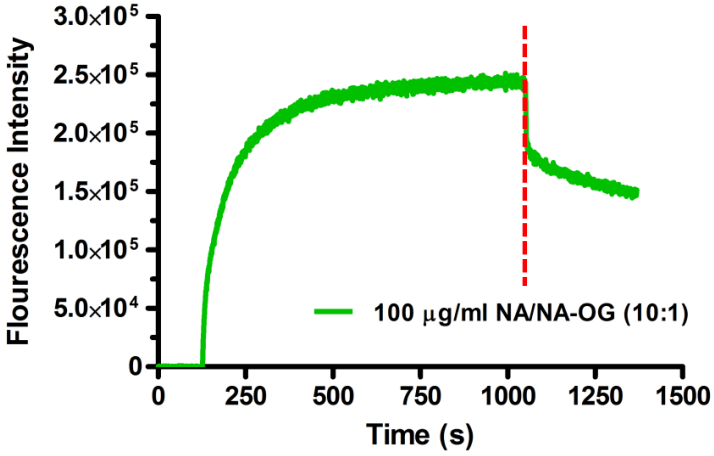

Figure 7.6. A TIRF spectrophotometer was used to test direct adsorption of neutravidin (NA) to a silica surface. This graph shows that adsorption takes ≈ 400 seconds using a solution with a 100 μg/mL concentration of NA. At the vertical dashed line solution without NA is washed through the chamber reducing some of the fluorescence intensity, but leaving a significant amount of surface bound NA.

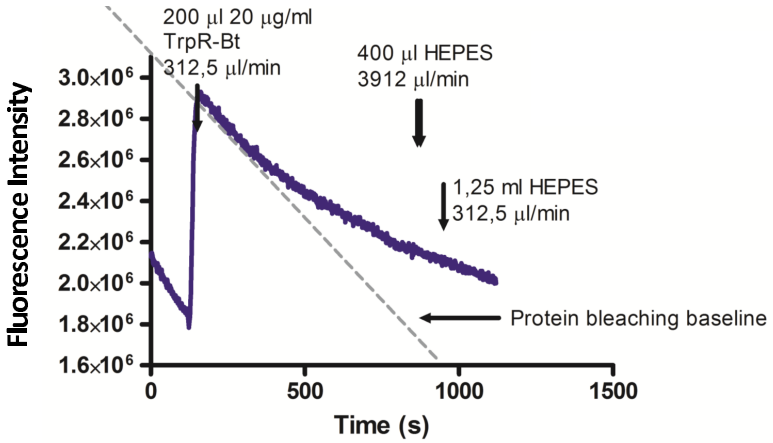

Figure 7.7. TIRF spectrophotometer measurement of neutravidin binding TrpR. The TrpR protein has no fluorescent label. Only a small inherent fluorescence is measured and rapidly bleaches. Compared to a bleaching baseline (dashed line), there seems to be binding of the biotinylated TrpR to the surface adsorbed NA. The protein is initially in solution at 20 μg/mL. After washing with HEPES buffer containing no protein, the TrpR stays bound to the NA.

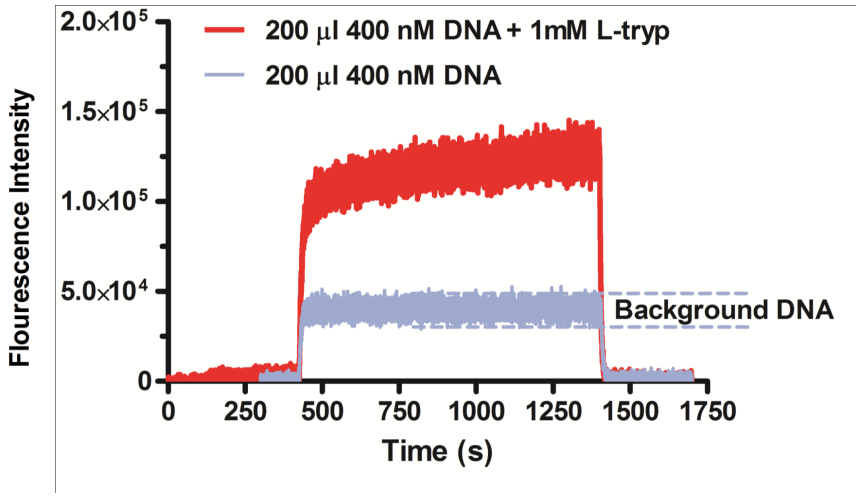

Figure 7.8. TIRF spectrophotometer measurement showing DNA binding to repressor with ligand compared to a background unbound DNA signal. With ligand there is the characteristic $1 - e^{-t/\tau}$ binding curve. Without ligand in solution the curve resembles a step function. This indicates that no binding is occurring, and that the signal is only background fluorescence from unbound DNA.

With the bulk binding assays, we have established several things. A gel-phase lipid bilayer was formed and the his-tag protein did bind to bilayer. Unfortunately, this binding wasn't stable on the hour long time scale that we need for the single-molecule assay and for the inchworm. Direct adsorption of NA works well as a method and the interaction between NA and biotinylated protein is long lasting. It is only a preliminary finding, but it appears that TrpR is still active when immobilized with this method (figure 7.8).

Single-molecule Assay Controls

Now we've established and tested a surface immobilization method that is effective and long lasting enough for our purposes. This can be used in our single-molecule

assay that was described earlier. Figure 7.9 diagrams this method with the NA adsorption method for protein immobilization. To determine if this method is feasible we did several control experiments.

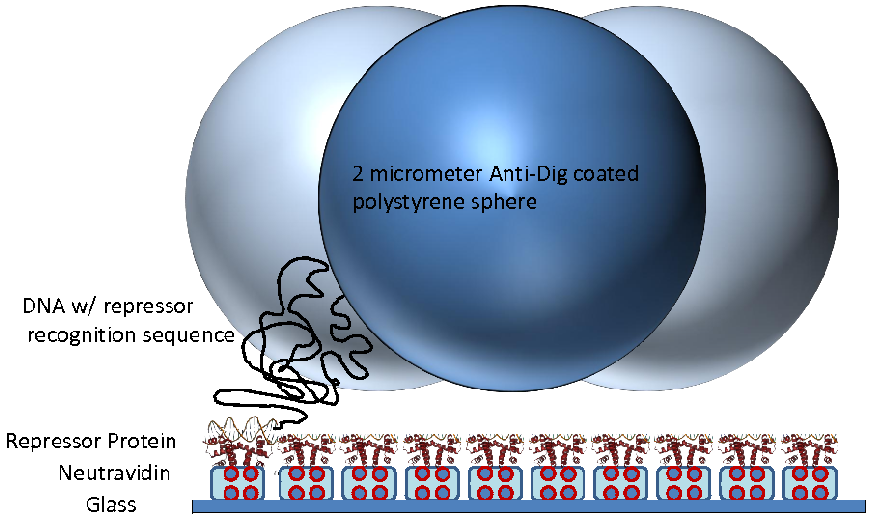

Figure 7.9. This cartoon diagram of the single-molecule assay shows the final surface immobilization method used. (Not to scale) NA is adsorbed directly to a piranha cleaned glass coverslip. The repressor protein is biotin labeled and this label binds to the NA. At the end of the DNA is the operator sequence for the particular protein. The 4062 base pair DNA used has a repressor binding sequence starting 7 base pairs from the end at each end. One 5' end has a dixogenin label. For the permanent tether assay: the protein is omitted and the free end of the DNA has a biotin label.

A permanent tether assay was used as a control of the method and analysis. With a permanent tether assay, we are able to observe tethered beads for long periods of time (tens of minutes). This allows us to determine if it is possible to differentiate between free diffusion and tethered diffusion without the complications of DNA-protein binding. The permanent tethers are formed by a biotin label on one end of the DNA binding to NA adsorbed to the surface, and a digoxigenin label at the other end

of the DNA binding to a digoxigenin antibody (anti-dig) coated microsphere. Details of the method follow. The microchannel is formed by sandwiching a piece of parafilm between a microscope slide and a coverslip. The parafilm has a channel cut out that lines up with an input and output hole drilled into the microscope slide. The coverslip has been cleaned by piranha etching (3 parts sulfuric acid to 1 part 30% hydrogen peroxide) for 30 minutes. The chamber is sealed by heating the assembled pieces until the parafilm melts using a hot plate. Several chamber volumes of dH_2O are flowed through. Neutravidin (NA, 100 μg/mL) in HEPES buffer (20 mM HEPES, 150 mM KCl, pH 7.8) is flowed into the chamber and allowed to incubate for 30 minutes to allow time for NA adsorption; this is done twice. Then the chamber is washed with HEPES buffer to remove any unbound NA. Casein (100 μg/mL) in HEPES buffer is added as a blocking agent to reduce nonspecific binding of the repressor proteins and DNA to exposed glass surfaces and is incubated for 30 minutes. Wash with HEPES buffer again to remove unbound casein. Buffer solutions are used in most biological assays. Most biological components are sensitive to pH and a buffer solution contains a weak acid and its conjugate base. This works to make the solution's pH change less if a strong acid or base is added. The salt concentration used in the HEPES buffer described is 150 mM which is about the same as the salt concentration inside a cell.

The microspheres used in this assay are 2.1 micrometer diameter, Anti-digoxigenin coated (Spherotech). To create bead-DNA constructs, the microsphere solution is first vortexed and sonicated thoroughly. 200 μL of bead solution is taken from a stock

solution and bovine serum albumin (BSA) is added to 100 μg/mL (aids in pelleting). Beads are washed two times by pelleting. Pellets are formed by centrifuging (3000g for 5 minutes), then to wash the pellet supernatant is pipetted out leaving about 10 μL of solution, 190 μL of HEPES buffer is added, then to disperse the pellet the solution is vortexed and sonicated again (first time only). After the second washing, the pellet is suspended in 50 μL of HEPES buffer. DNA is added and incubated two hours with gentle shaking. The DNA used has a biotin label at one 5' end and a digoxigenin at the other 5' end.

After incubation the bead-DNA constructs are injected into a microchamber prepared as described previously, and allowed to incubate for 10 minutes with the coverslip side facing down. This allows the slightly negatively buoyant beads to settle close to the coverslip surface and gives time for the biotin-NA bond to form resulting in more tethered beads per area. The microchamber is set up in a 100x objective brightfield microscopy system with images recorded at 100 Hz at 320x240 pixel resolution (The field of view is about 53x40 microns). Permanent tethers in the field of view are recorded for about ten minutes. There are typically only two or three tethers in the field of view at a time. This isn't many, but it could be optimized for real experiments measuring the protein unbinding time. The recorded images are analyzed according to the algorithm described in appendix B.

Figure 7.10 shows the results of the assay described above. There are 40 recorded trajectories, each recorded for about ten minutes. This gives about 6×10^4 data points

for each trajectory. RMS fluctuations are calculated by a sliding window method:

$$x_i^{RMS} = \left[\left(\sum_{j=i-n/2}^{i+n/2} \left[x_{j+1} - x_j \right]^2 \right) / n \right]^{1/2} . \qquad \text{(VII.5)}$$

Where n is the size of the sliding window. For these controls $n = 100$. All values reported are the x_i^{RMS} value divided by the time in between data points, 10 ms. The values of this calculation for each trajectory are binned into 100 bin histograms. There are three clear regimes of data. The grouping with peaks less than 1 nm/ms are interpreted as microspheres that have nonspecifically bound to the surface; they are "stuck". The recorded RMS fluctuation in this case is the measurement noise of the system. This was determined by tracking a dust speck on a dry slide. Any recorded movement of the speck would be due only due to setup vibration or measurement error, not diffusion. There are 5 stuck trajectories. These were the only stuck trajectories recorded. Another regime peaks around 6-7 nm/ms. For a 2.1 μm diameter bead at room temperature the average fluctuation for 10 ms is calculated to be 65 nm ($\sqrt{2Dt}$ for $D = 0.2$ μm^2/s, $t = 10$ ms). Since data points are recorded each 10 ms in the experiment and these trajectories are peaking between 60-70 nm fluctuations, this agrees well with the measured value and this regime is interpreted as freely diffusing beads. There are 20 freely diffusing trajectories. The third regime has peaks ranging from 2-4 nm/ms. There are 13 of these trajectories. The controls explained in the following paragraphs provide evidence for the interpretation of this regime as tethered beads. There are two remaining trajectories that peak at about 1.5 nm/ms. These could be beads with more than one DNA tether (further restricting the

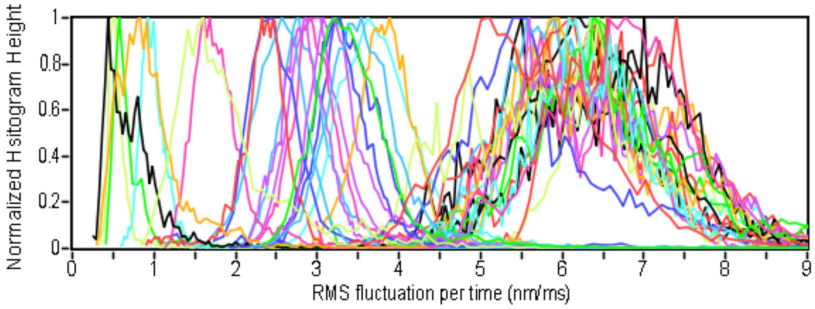

Figure 7.10. Normalized histograms for 40 trajectories are shown on the same axes. This is data from the permanent tether assay. While confusing to look at, the purpose of this is to show that in fig. 7.11 and 7.12 the peaks represent different regimes of SM trajectories. None of the SM trajectories are bimodal. The trajectories peaking below 1 nm/ms are understood to be stuck beads, peaks above 5 nm/ms are understood to be freely diffusing beads, and 2-4 nm/ms are understood to be tethered beads. These measurements are for fluctuations measured at intervals of 10 ms and are averaged using a sliding window method with a width of 1 second. The controls in fig. 7.11 and 7.12 agree with this interpretation.

tethered motion), or nonspecifically bound stuck beads that are more loosely bound than the majority of stuck beads.

The first set of controls were to remove a crucial portion of the DNA-biotin-NA binding complex and observe what happens to the observed distribution of RMS fluctuations. The expected outcome being that stuck and diffusing beads would remain and that the tethered regime would disappear. In one control DNA lacking a biotin tag was used. In another control NA was not adsorbed to the surface. In both cases the same preparation and data taking protocol as the permanent tether assay was used barring the obvious changes (DNA with no biotin tag was used in one control, and skipping the NA adsorption step in the other). Figure 7.11 shows the results for these two controls and includes the data for the permanent tether assay

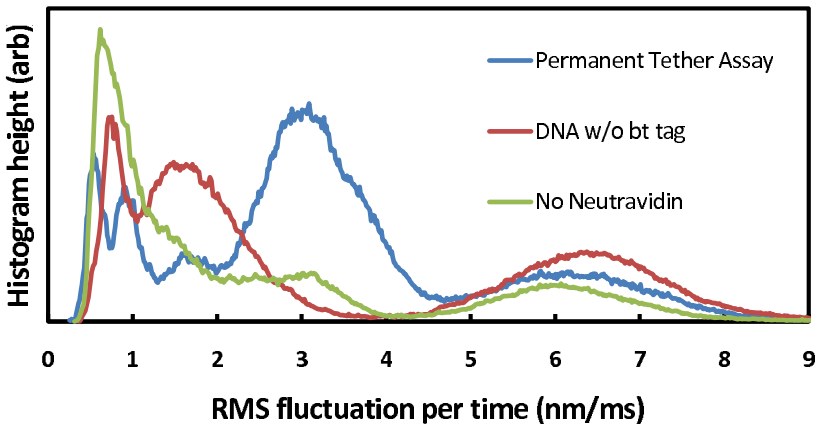

Figure 7.11. This histogram is produced by using the RMS fluctuation data for all the SM trajectories without discriminating between different trajectories. The permanent tether assay (blue) (same data as figure 7.10 is compared with two controls: an assay with DNA lacking a biotin tag (red), and an assay with no NA adsorbed to the surface (green). All three assays contain peaks for stuck and freely diffusing beads. The two controls show a greatly reduced center peak.

also shown in figure 7.10. For this figure data was calculated in the same way, except that the RMS fluctuations were collected into one histogram instead of a histogram for each trajectory. This simplifies the graphs while still allowing the three regimes to be identifiable. As in figure 7.10 all trajectories still form unimodal Gaussian-like histograms. For the control omitting a biotin tag on the DNA there is no tethered regime observed. For the control with no NA adsorption, there is a small peak there, but it is greatly reduced compared to the permanent tether assay. Without NA, there isn't specific binding of the end of the DNA to the surface, but there is still a possibility for unspecific binding anywhere along the DNA. This is reduced by the casein used in the preparation protocol, but unspecific binding is not completely eliminated.

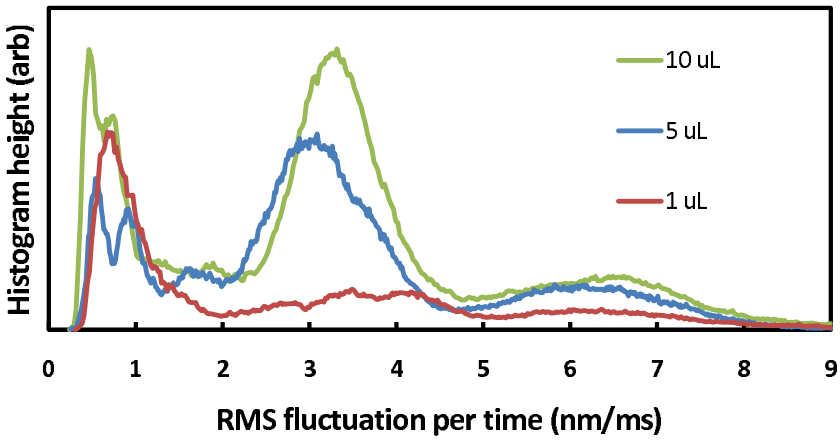

Figure 7.12. As another set of controls, the concentration of DNA during the bead-DNA incubation step was varied. 1, 5, and 10 μL volumes of DNA are used from a stock solution of DNA at a concentration of 3 ng/μL. Expected results are seen. The peak corresponding to the tethered state grows with increased DNA. If the peak moved towards smaller RMS fluctuations this would indicated multiple tethers on the same bead. This is not observed.

Another set of controls varied the concentration of the DNA during the bead-DNA incubation stage. This leaves the DNA-biotin-NA binding complex intact, but changes the amount of biotin labeled DNA to attach to the NA. The same protocol was used as in the other assays except that the amount of DNA in the incubation stage was varied (1, 5, or 10 μL from a stock solution of DNA at a concentration of 3 ng/μL). The results (figure 7.12) show a correlation between the concentration of DNA and the size of the tethered regime peak.

An interesting detail to keep track of with this assay and with TPM assays in general is that a Brownian particle tethered to a surface exerts a force on its tether, on average. This means that the unbinding reaction being observed is not truly at zero force. The physical size of the Brownian particle causes a volume-exclusion effect

which stretches the tether, an entropic spring. Reference [83] calculates this force for an equilibrium system and finds, in the case of a Gaussian-chain model, the effective force:

$$\langle F_{\text{eff}} \rangle = \frac{kT}{\sqrt{\pi l \xi / 3}} \left(\frac{1 - e^{(-N_r^2)}}{\text{erf}(N_r)} \right). \tag{VII.6}$$

Where l is the contour length of the tether, ξ is the persistence length, and N_r is a dimensionless number defined as $r/\sqrt{l\xi/3}$. For this experimental setup, $l = 1.38$ μm, $\xi = 50$ nm, and $N_r = 6.92$, which gives $\langle F_{\text{eff}} \rangle = 15$ fN. This is relatively small, but not insignificant compared to the pN scale force that is relevant to most molecular motors.

Analysis of Trajectories to Find Unbinding Times

The permanent tether assay with its controls establish that we can differentiate between microspheres undergoing free diffusion or tethered diffusion. The next step is to measure how accurately we can determine the transition point between these two states. A method called Page's test [84] by determining the transition points can be used to find the unbinding times of the DNA repressor. The unbinding time is the time that elapses between the diffusive to tethered transition and the tethered to diffusive transition. Page's test is concerned with the fluctuations in the position measurement over time. For each data point a function is calculated for the tethered

and diffusive states, $f_{teth}(x,\sigma)$ and $f_{free}(x,\sigma)$, where:

$$f(x,\sigma) = \frac{1}{(2\pi\sigma)^{1/2}} exp\left\{\frac{-(x-\bar{x})^2}{2\sigma^2}\right\}. \tag{VII.7}$$

Where the running mean, $\bar{x}$, is calculated as follows:

$$\bar{x}_i = \left(\sum_{j=i-n/2}^{i+n/2} x_j\right)/n. \tag{VII.8}$$

The value of the width of the function, σ, for the tethered and free states, is determined from the permanent tether assay experiments. Next, the log odds ratio of the tethered and free functions is calculated:

$$g(x) = log\left(\frac{f(x,\sigma_{att})}{f(x,\sigma_{det})}\right), \tag{VII.9}$$

and the Page's test is applied:

$$PT_i = \sum_{j=0}^{j=i} Max\left\{g(x_j), 0\right\}. \tag{VII.10}$$

Equation VII.7 is the probability density for x to be in a particular state, free diffusion or tethered. The log of the ratio of the two probability densities (equation VII.7) is positive when the ratio is greater than one (more likely to be in the tethered state) or negative when the ratio is less than one (more likely to be in the free diffusion state). Equation VII.10 creates a running total that stays near zero while in the free state, gradually increases while in the tethered state, and quickly decreases back to zero once back in the free state. There is an obvious peak at the transition from tethered to free. If this test is applied in the opposite direction of time it gives an

obvious peak at the transition from free to tethered (see figure 7.13). With both of these transitions, the unbinding time of the protein, τ_{off}, can be calculated from the time elapsed from transition to transition. The calculation is done separately in the x and y direction. The measured unbinding time is the average of the unbinding times found in each direction. Page's test is applied only to data showing a transition from free to tethered and back to free. In experiment, beads in the stuck state never release from the surface and therefore would not be included in the analysis.

Because we do not have data of actual repressor protein unbinding events, τ_{off}, it was necessary to create artificial data sets of binding events to examine the effectiveness and accuracy of the Page's test analysis method. This was done programmatically by linking together diffusive and tethered data sets from the permanent tether assay. The data starts with a microsphere in a diffusive state, it switches to being tethered, and then switches back to being diffusive (see figure 7.13). This resembles the expected data from the microsphere-DNA construct interacting with the surface immobilized repressor protein in the single-molecule experiment. The artificial data sets are generated with a specified unbinding time, t_{off}, that is modified by adding a random amount from 0 - 10% of t_{off}. The random amount is added so that we don't know the exact expected τ_{off} when using the algorithm. This final unbinding time is recorded and compared to what is found by applying Page's test to the data.

One of the benefits of the Page's test is that it has very few free parameters. The only parameters are: σ_{free}, σ_{teth}, and the size of the running mean window n. Both

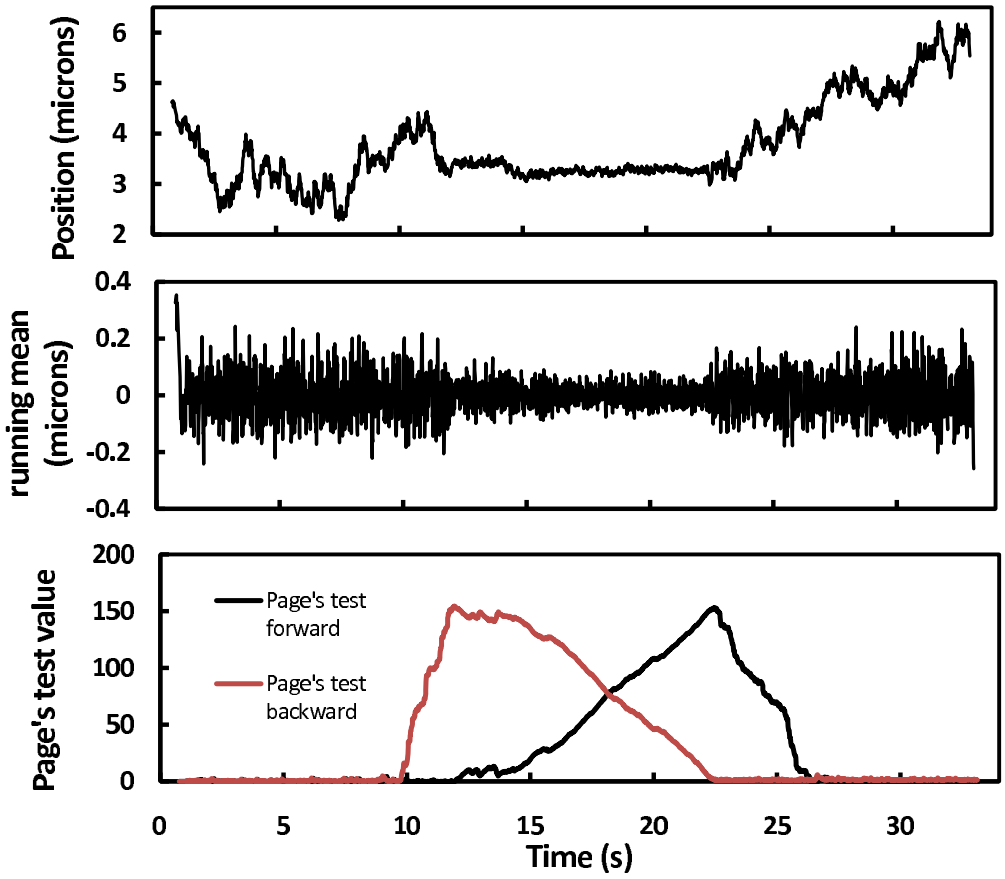

Figure 7.13. The top graph shows a trajectory from one of the artificial binding sets. It shows a microsphere diffusing, binding to the surface via the DNA tether, then unbinding and freely diffusing again. The middle graph shows the trajectory mins the running mean (equation VII.8) of the microsphere trajectory with a sliding window size of $n = 15$. Applying Page's test to the trajectory from left to right results in the black curve on the bottom graph. Applying it from right to left results in the red curve. The peaks of these curve mark the transition from diffusing to tethered and the transition of tethered to diffusing. In this example Page's test found an unbinding time of 10.35 seconds and the actual unbinding time was 10.5 seconds.

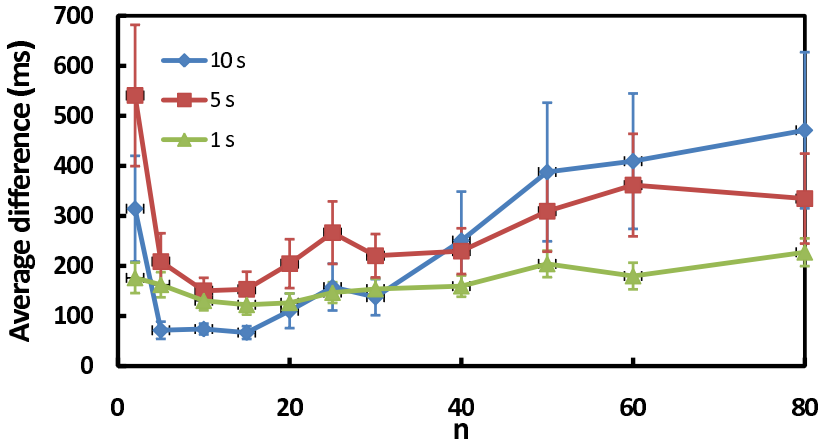

Figure 7.14. Accuracy of Page's test method for varying sliding window size. On the vertical axis is the average difference between known and measured unbinding times found from the Page's test method outline in the text. Results are found from averaging over 30 unbinding events. The results are similar for unbinding times of 10, 5 or 1 seconds. The best accuracy is found at $n = 15$. Error bars represent one standard deviation of the mean.

σ_{free} and σ_{teth} are determined by the control data. They can be calculated by fitting a Gaussian to the histogram of the diffusive motion of the tethered beads from the permanent tether assay. The only truly free parameter is n. We can pick a value of n by finding what value results in the best accuracy with the data sets. Accuracy of Page's test for varying n was found using the artificial data sets described in the previous paragraph. Results are shown in figure 7.14. Data sets with τ_{off} of about 10, 5, and 1 seconds were used. There were 90 total data sets. The best accuracy is found at $n = 15$ with the unbinding measurement error being 66 ± 13 ms at 10 second unbinding time, to 150 ± 35 ms at 5 second unbinding time, and 122 ± 20 ms at 1 second unbinding time. For unbinding times less than one second the Page's test method did not reliably pick out the unbinding events.

Conclusions

Controls from the permanent tether assay show that the difference in tethered and diffusive motion of the microspheres is experimentally observable using a 100x objective with brightfield microscopy and a 100 Hz camera. Using artificial binding data sets, we showed that Page's test works as a method to find unbinding times, for unbinding times greater than one second. For this data, the method is most accurate at a sliding window averaging width of $n = 15$. The accuracy at this value of n for the unbinding time is about 100 ms. It is likely that accuracy could be improved through the use of a faster frame rate or smaller (more quickly diffusing) microspheres. This assay would be useful to measure unbinding times of DNA repressor proteins. The parallel nature of the measurement could allow data collection to happen much more quickly than an exclusively one molecule at a time single-molecule experiment. In the permanent tether assay, there were only a few tethers in the same field of view at one time. This should be able to be improved by increasing the concentration of the bead-DNA constructs. There is a limitation though. If the concentration is too high then beads will pass over or interact with each other often, and this can confuse the tracking algorithm. The simple nature of the experimental setup allows this to be done at a low cost. This assay could be extended to measure the unbinding times in the presence of a force. The force could be controlled by introducing a steady flow in the microchamber which would exert a force on the microsphere.

CHAPTER VIII

CONCLUSIONS AND OUTLOOK

Feedback Ratchet

The feedback ratchet was successfully implemented and demonstrated the predicted increase in average velocity compared to the periodic ratchet (figure 5.5). Two feedback algorithms were compared, MIV and MND. Our MND method was shown to be a small improvement in experiment since there was a nonzero implementation delay time, τ, (figure 5.9) of about 5 ms. When including the complications of effective ratchet potential and implementation delay time there is a good agreement between experiment and simulation (simulations done by Nathan Kuwada) (see figure 5.6). The MND method achieves this improvement by adjusting a parameter x_0. In an unexpected result, x_0 maximizes transport when it is equal to the expected diffusion distance over the implementation delay time (when $x_0 = \sqrt{2D\tau}$, seen in figure 5.8).

This setup could be used to do a Maxwell's Demon type experiment. A flat potential with a controllable barrier could be easily created. It would separate the flat potential into two halves, A and B. The feedback can be used to only allow particles, for example, to go from A to B, but not B to A. There are several interesting relationships that could be examined. One, by increasing the implementation delay

time the effectiveness of the Demon would be reduced. For a system with Brownian motion, as τ increases the information being used to make a decision is increasingly irrelevant to state of the system when the decision is finally implemented. Varying τ would be an experimental measure of this. Another interesting relationship could be tested by introducing a sloped potential instead of a flat potential into the Maxwell's Demon setup. This would exert a constant force on the particles. This force could oppose the sorting of the Maxwell Demon. By varying the force one could find a stall force, similar to a molecular motor, where the average number of particles on each side of the barrier stays the same. This could provide a measurement of a type of "effective force" of the Demon.

There is an intriguing behavior of the effective ratchet potential, V_{eff}, calculated by equation V.10. As the ratio of diameter to period length increases the equation predicts that the asymmetry decreases and eventually switches direction (see figure 8.1). It would be an interesting experiment to test this and see if the prediction is true. If it worked, this would allow the optical ratchet to sort microspheres by size. Those microspheres below the critical ratio of d/L (0.7 from the calculation) would be transported in the preferred direction of the ratchet, and those above the critical ratio would be transported in the opposite direction. The critical ratio could be easily tuned by adjusting the length of the periods. This could have applications for sorting of micrometer sized particles.

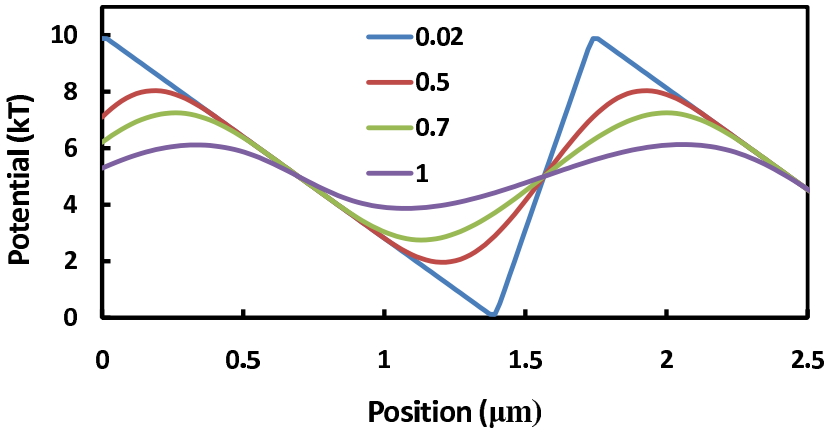

Figure 8.1. The key gives the ratio of diameter to period length, d/L, for each curve. The period in this plot is the value from the feedback ratchet experiments, 1.74 μm. For a $d/L = 0.7$ (green curve) there is no asymmetry. For larger values the asymmetry is in the opposite direction as the input potential. $d/L = 0.5$ is equivalent to that in the feedback ratchet experiment.

To tie the two main themes of this thesis (feedback ratchets and molecular motors) together a little bit, it is worth mentioning that feedback ratchet systems have some surprisingly strong connections to molecular motors. For a certain form of kinesin (KIF1A), its monomeric form can still achieve transport on a microtubule and hydrolyze ATP. It does this with a slower net speed and lower efficiency compared to the dimeric form of KIF1A. The observed movement can be modeled by a stochastic flashing ratchet mechanism [85]. The motion of the dimeric version of this protein can be modeled as a feedback ratchet system [86]. In the dimeric form stepping is gated, this allows the stated gains in efficiency and speed. This is a form of feedback. It is a feedback system where kinetic rates of the two heads of kinesin depend on the chemical state of the other head.

Parallel Single-molecule Assay

The single-molecule TPM-like experiment described in chapter VII was found to be feasible. Using a permanent tether assay that substituted a biotin-neutravidin link instead of a DNA-repressor protein link, we showed that there was diffusive tethered motion of the microsphere and that this could be differentiated between both free diffusion and nonspecific binding to the surface. This assay can be used to measure a distribution of τ_{off} with and without ligand present for the three repressor proteins used in the TW and IW motors. Currently work is being done to engineer the proteins to have a biotin tag attached in a specific place that doesn't interfere with ligand or DNA binding, then the single-molecule assay should be functional. Once the distribution of τ_{off} is measured that can be converted into an unbinding rate, k_{off}. Simulations of the TW are being done. With experimentally measured values for the parameters of repressor binding added to the simulation, there will be few free parameters in the model. Similar to the simulations of myosin-V done by Erin Craig [62] the simulation could be a very accurate predictor of the behavior of the TW motor. Similar simulations could be done for the IW motor.

One of the potential experimental complications of the TW motor is that it might have to walk against a slow current. This current might be necessary to introduce the changing ligand concentration that coordinates the feet binding. The single-molecule assay could be extended to measure the kinetics of the repressors under force by

introducing a current into the microchamber. A current would exert drag on the microsphere and exert a force on the DNA-repressor linkage. By varying the speed of the current, τ_{off} versus force could be measured.

The TW motor is currently being worked on in the Linke lab along with the rest of the collaborators, and the IW motor is being done exclusively by the Linke lab. Hopefully soon we will read about the successful observations of stepping motion of both of these artificial molecular motors.

APPENDIX A

DESCRIPTION OF MOLECULAR BIOLOGY TECHNIQUES USED

Plasmid Transfection

The pET15(b) vector has been modified to carry each DNA repressor with a HIS-TEV fusion at the N-terminus.

The Top10 (Invitrogen) strain of E. Coli is used for DNA manipulation and propagation. 1 μL of DNA is incubated with one aliquot of chemically competent BL21(DE3) for 30 minutes on ice. Cells are heat shocked at 42°C for 30-45 seconds. Cells are incubated on ice for at least 5 minutes. 200 μL of SOC medium is added and transformed cells are incubated at 37°C and 220 rpm for 1 hour.

Cells are plated out onto L-agar supplied with ampicillin (50 μg/mL). 20 μL and 200 μL samples are spread onto the plates with a plating tool. Plates are incubated at 37°C overnight. Do not seal plates, this allows an ample oxygen supply for the bacteria.

Protein Expression

For protein expression, the BL21(DE3) (Invitrogen) strain of E. Coli is used.

A single colony of transformed E. Coli is picked from a fresh plate and grown overnight at 37°C and 220 rpm in 5 mL of LB media supplemented with the appropriate antibiotic. The next day, a glycerol stock can be prepared from the overnight culture by adding 500 μL culture to 500 μL of 40% glycerol, mixing and storing at -80°C.

Cultures are started by diluting 1:1000 overnight culture to LB media supplemented with ampicillin (50 μg/mL). A typical culture size is 2 L total. This is done in five separate 400 mL cultures each in a 2 L flask. It is important to leave about 80% of a culture flask empty to allow enough oxygen for the E. Coli to grow. Cultures are grown at 37°C and 220 rpm. Growth is monitored by measuring optical density (OD) at 600 nm. Be sure to use sterile LB medium as the blank for OD measurements.

Once the OD reaches 0.6-1 the culture should be induced with 1 mM IPTG. The culture reaches this level in about 4-6 hours. Once induced the protein expression should be allowed to carry out for 3 hours at 37°C and 220 rpm. Cells are harvested by centrifugation at 4000 g for 20 minutes. Cells are washed with phosphate buffered saline (PBS) pH 7.4 and centrifuged at 4300 g for 15 minutes. PBS is discarded and cell pellets stored at -20°C until required.

Protein Purification

SDS-PAGE is carried out on samples from each step of the purification process. Use 10% Tris-BIS precast gels using MES buffer.

A cell pellet is thawed and resuspended into 30 mL of 50 mM potassium phosphate,

pH 7.8, 0.5 M NaCl, 0.5 mM DTT (referred to as Binding Buffer). Protease inhibitors are added (Complete protease inhibitor cocktail from Roche). The suspension is passed through a pre-chilled french press three times and the resulting crude lysate centrifuged at 30,000 g for 20 minutes at 4°C. To the supernatant, 5% of polyethylene imine (PEI) in aqueous solution pH 7.5 is added dropwise to a final concentration of 0.1%. The mixture is stirred for 10 minutes at 4°C, then centrifuged at 30,000 g for 20 minutes at 4°C. The resulting supernatant is kept on ice until nickel-affinity chromatography.

A plastic column is prepared with 2-3 mL of nickel affinity resin (Qiagen NiNTA) and equilibrated with 10 volumes of binding buffer. The protein supernatant is passed twice through the column, and the column is then washed with 20 mL of binding buffer. The column is further washed with 20 mL of wash buffer (binding buffer with 30 mM imidazole). Protein is then eluted with 20 mL of elution buffer (binding buffer with 0.5 M imidazole). Use concentrators to replace buffer with binding buffer.

Size-exclusion chromatography is carried out using a high pressure liquid chromatography (HPLC) system. A Superdex S200 (GE Healthcare) column is equilibrated with size-exclusion buffer (20 mM HEPES, pH 7.5, 0.15 M KCl, 0.5 mM DTT). Protein is passed through (0.5 mL load per run) at 0.5 mL per minute. 1 mL fractions are collected. After chromatography is finished, the appropriate fractions (those containing the repressor protein) are collected and concentrated using MWCO 10 kDa Centriplus concentrators. Concentration of protein is measured at 280 nm

in a spectrophotometer. Protein is aliquoted in 100 μL samples and flash frozen in liquid nitrogen and stored at -80°C.

The above protocol leaves the His-tag on the protein. The His-tag can be removed with TEV protease. This process starts before the size-exclusion step. The protein solution is dialyzed against 1 L of dialysis buffer (50 mM Tri-HCl, pH 8.0, 0.15 M NaCl) for 2 hours using a MWCO $<$ 10 kDa membrane. DTT and EDTA are added to final concentrations of 0.5 mM each. Protein concentration is measured using absorption at 280 nm and TEV protease is added at 1:50 concentration relative to the protein. Cleavage is allowed to proceed overnight at room temperature. The protein solutions is again concentrated into binding buffer using Centriplus concentrators. The nickel-affinity chromatography is then repeated. After this size-exclusion chromatography can be performed.

DNA Methods

When working with DNA it is important to use sterile technique. Restriction enzymes come from bacteria, so avoiding bacterial contamination is necessary. The following will help avoid contamination: clean your working space and pipettes with 70% ethanol, use sterile eppendorf tubes, wear gloves at all times and sterilize often with 70% ethanol, use sterilized buffer and dH_20, and use sterile pipette tips with filters in them.

TAE buffer is 40 mM Tris-Acetate and 1 mM EDTA at pH 8.5. Loading buffer for DNA gels is 3 grams sucrose and 0.035 Orange-G dissolved in 10 mL TAE buffer.

DNA gels used for kilobase or longer DNA fragments are 0.6% (w/v) agarose. To make 150 mL of gel solution dissolve 0.9 g of low melt agarose in 150 mL of TAE buffer by boiling solution in the microwave (1-2 minutes). The solution will be very hot. Let it cool down so that you can touch the beaker, but keep swirling beaker during this time to keep an even temperature throughout the volume. Add 6 drops of Ethidium Bromide (1 mg/mL) in fume hood. Place comb in mold and cast the gel. The gel can be used after at least a half hour of setting time, preferably 1 hour.

DNA digestion

Due to high variability of restriction quality and activity, the first step in DNA digestion is to check the efficiency of your restriction enzyme. Use the manufacturer's guidelines as a starting points, but expect to make adjustments. Try to digest 1 μg of λ-DNA with 1U, 5U, and 10U of enzyme. 1U of enzyme is defined to digest 1 μg of λ-DNA in 1 hour at 37°C in 50 μL of reaction buffer, but your results may vary significantly from this. Mix 50 μL samples of the reaction with appropriate buffer, λ-DNA, and sterile dH_20. Incubate samples for 2-4 hours at 37°C. After incubation store samples on ice. Cast a DNA gel and pour TAE-buffer into the electrophoresis tray. Prepare the digested λ-DNA (10 μL of sample with 10 μL of sterile TAE buffer), Hind III digest ladder sample (1 μL of ladder and 19 μL of TAE buffer), and undigested λ-DNA (1 μL of DNA and 19 μL of TAE buffer). Gently vortex

the samples, quickly spin them down, and incubate at the inactivation temperature for 20 minutes. This incubation denatures the enzymes and denatures any secondary structures of the DNA. After the incubation, mix each sample with 5 μL of loading buffer and load 25 μL samples into the wells of the gel. Run the gel at 30V for 20 minutes, and then 70V for one hour. Check the gel on a UV table and image it. If bands are not well separated, run the gel for a longer period of time.

Now it is known what concentration of enzyme results in a satisfactory digest of the DNA. Using that concentration, a large batch (10 times the efficiency check) will be digested. Include a negative control. After digestion cast a gel and run gel until good separation of desired bands is achieved. The next step is to cut out the portion of the gel with the desired DNA band. A UV table can easily cause skin and eye damage. Use UV protective glasses and cover all exposed skin while cutting DNA gel. Place all gel into dialysis tubing (MWCO of 6-8 kDa) with about 2 mL of TAE buffer. The gel should be placed straight on one side of the tubing. Avoid bubbles in the tubing. Close the tube with clips. Place the tubing with gel in the tubing is closest to the black electrode. Run the electrophoresis equipment at 70V for 30 minutes. Using the UV table, check that all DNA has left the gel and entered the buffer. Carefully pipette the DNA solution into a falcon tube. Concentrate the DNA using 1.5 mL concentrators. Use two concentrators. Spin some water through the tubes at 500 g for 5 minutes. Don't let the filter run dry at any time. Discard the water and add 500 μL of sample to each filter device and centrifuge at 500 g for 15

minutes. Add more sample to the filter and centrifuge again. Continue this process until all the DNA has been concentrated. When the DNA is concentrated, take a new Eppendorf tube, add 10 μL of water to the tube, turn the tube filter upside down and spin 3 minutes at 1000 g.

DNA ligation

The oligos that will be ligated to the length of DNA from the digest must first be annealed to each other. Commercial oligos are shipped as single stranded DNA without a 5' phosphate. Polynucleotide kinase (PNK) is an enzyme that catalyzes the transfer of a phosphate from ATP to the 5' end of either DNA or RNA. To anneal the primers use 4.5 μL of 100 pmol/μL of each ssDNA oligo. Add 1 μL of 10x PBS buffer. To anneal the primers, heat them to 95°C for 5 minutes. Lower the temperature to 80°C and then lower 3°C each 5 minutes until you reach 50°C. Use the thermocycler to do this.

To the concentrated lengths of digest DNA add: ligase buffer to 1x concentration, 2 μL of E. Coli ligase, 1 μL of each annealed oligo, and 1 μL of PNK enzyme. Ligate the DNA overnight at 16°C. Inactivate the ligase by heating it to 65°C for 30 minutes. Purify the ligated DNA by using the spin concentrators. Run a gel to confirm presence of correctly sized DNA.

Bilayer Bulk Binding Protocol

1. Flush out excess vesicles with water (3-4 chamber volumes)

2. Check for gel-phase lipid bilayer formation (FITC filter), save image. There will be uniform fluorescence and a bleached spot will recover in about 10 minutes
3. Flow in Nickel buffer (3-4 chamber volumes), let incubate a few minutes
4. Flush out unbound nickel with pure water (3-4 chamber volumes)
5. Flow in BB (3-4 chamber volumes)
6. Flow in a solution of protein + BB (2 chamber volumes), let incubate a few minutes
7. Flush out with ligand + BB to remove unbound protein
8. Flow in ligand + DNA +BB (2 chamber volumes), let incubate a few minutes
9. Flush out unbound DNA with ligand + BB (2 chamber volumes)
10. Check for lipid-protein-DNA binding (Texas Red filter), save image. There will be uniform fluorescence only near the inner surfaces of the microchamber.
11. Flow in BB with no ligand (2 chamber volumes), let incubate a few minutes. DNA should unbind without ligand present.
12. Flush out unbound DNA with BB (2 chamber volumes)
13. Check for unbinding, save image. No fluorescence with the Texas Red filter.
14. Check for rebinding. Repeat steps 8-13

APPENDIX B

PARTICLE TRACKING ALGORITHMS

For Feedback Ratchet Experiment

For the case of particle tracking in real time for the feedback ratchet experiment it is important for the computation time to be as short as possible. Therefore the algorithm is designed to be as simple as possible. Images, 200 pixels by 50 pixels, are captured at 130 frames per second. Particles appear as bright circles within the field of view. The image is thresholded so that only these bright circles are left. A centroid is fit to each of the bright circles (1 to 4) in each image. Each position is ranked by y-value and particle trajectories are assembled assuming that particles do not pass each other. The position determined for each particle by the algorithm is marked on the image with a colored circle. This entire process takes about 4 ms.

For Single-molecule Repressor Binding Experiment

Particle tracking

Images are captured at 100 frames per second at 8-bit grayscale. The image size is 320 pixels wide by 240 pixels tall. Image analysis is done in LabVIEW after the experiment is completed.

The first step of image analysis is to compute a Fast Fourier Transform (FFT) of the image. Then frequencies below 5 (pixel noise and small objects) and above 45 (brightness variations over large regions of image)are removed. The inverse FFT is calculated and that is the new filtered image, which is saved to an image buffer. To find the particles this image is thresholded at a brightness of 35, setting to 0 or 1 all pixels with a brightness below or above 35 respectively. The LabVIEW function 'Remove particle' is used to remove all identified particles too small to be microspheres. The positions of the remaining particles are calculated. Since the 8-bit image is reduced to binary after the thresholding stage a centroid calculation would be less accurate than it could be. To get sub-pixel accuracy, the image saved to a buffer is retrieved, and the center of a region of interest (ROI) is set to the particle positions from the binary image. In each of these ROI's the centroid is measured. For the setup used in the single-molecule experiment in this thesis, this algorithm gives a measurement error with a standard deviation of 10 nm for a fixed particle.

Position to trajectories

While the idea of linking successive particle positions is simple, implementing it in software can be complicated. Starting with an array of particle positions in each frame, the first step is to pick a particle in the first frame. Let's call that particle A_1, where 1 indicates that it is the first position of that particle. Then the distances between particle A and all the particles in the next frame are calculated. If the closest particle is within five pixels that one is considered the next position in the trajectory,

A_2. If all the calculated distances are greater than five pixels then none are considered to be particle A, and particle A was not tracked in that frame. The next frames are checked successively and if there are 50 frames in a row without finding Particle A, then that is considered the end of the trajectory. All the positions found for particle A are placed into an array for trajectories and deleted from the position array.

Starting back at the beginning of the position array, the next unlinked particle position is selected and the process is repeated to find the trajectory for particle B. This is repeated until all positions have been linked into trajectories. Final trajectories with less than 100 data points are ignored.

APPENDIX C

AXIAL FORCE CALCULATIONS

The theory used for the calculations in this appendix follow from reference [21].

Important Variable Definitions

Size parameter: $\beta = \kappa a$ ($\kappa = 2\pi n_1/\lambda_0$ = wavenumber in a surrounding medium with an index of refraction n_1, λ_0 = wavelength of laser in a vacuum.) Mie coefficients a_j and b_j are the scattering amplitudes of the for electric and magnetic multipoles. $\eta = \eta_2/\eta_1$, where η_2 is the refractive index of the microsphere.

Axial Force of a Single Optical Trap

In this calculation the laser beam is represented as a superposition of plane electromagnetic waves. The field scattered by the particle is a superposition of Mie fields; each field corresponds to one of the vectors of the plane waves that make up the laser beam. The beam is assumed to be circularly polarized. This sets the optical force field to be symmetrical under rotations around the beam axis.

The Maxwell stress tensor can be used to calculate the force of the laser beam on the microsphere:

$$\mathbf{F} = \lim_{r\to\infty}\left[-\frac{1}{2}\int_{S(r)} \mathrm{d}\Omega\mathbf{r}\left(\varepsilon E^2 + \mu_0 H^2\right)\right]. \tag{C.1}$$

A dimensionless force that doesn't depend on the input laser power, $\mathbf{P}$, will be used:

$$\mathbf{Q} = \mathbf{F}c/\eta_1\mathbf{P}. \tag{C.2}$$

$\mathbf{Q}$ can be thought of as an efficiency of momentum transfer from the field to the particle. In the case of a perfectly reflective mirror and a normal-incidence plane-wave, $\mathbf{Q} = 2$. $\mathbf{Q}$ can be split into two elements such that $\mathbf{Q} = \mathbf{Q}_e - \mathbf{Q}_s$. $\mathbf{Q}_e$ represents the momentum removed from the beam, and $\mathbf{Q}_s$ represents the momentum lost to the interference between scattered and incident beams. The difference between the two, $\mathbf{Q}$, is the momentum transfered to the microsphere.

Optical trapping in the directions transverse to the optical axis is easy. However, trapping in the direction of the optical axis, z, is more difficult. In this case the gradient force pulling the microsphere towards the focal spot must be larger than the force of laser propagation. The interesting calculation to do in this case is to calculate the force, along the z-axis, on the microsphere for different indices of refraction.

The momentum in the z-direction lost to interference can be calculated as:

$$\begin{aligned} Q_{sz} = \frac{8\gamma^2}{A}\mathrm{Re}[\sum_{j,m} \frac{\sqrt{j(j+2)(j-m+1)(j+m+1)}}{j+1}(a_j a_{j+1}^* + b_j b_{j+1}^*) \\ \times G_{j,m}G_{j+1,m}^* + \frac{2j+1}{j(j+1)} m a_j b_j^* \left|G_{j,m}\right|^2]. \end{aligned} \tag{C.3}$$

The total momentum taken out of the beam from the interaction with the microsphere can be calculated as:

$$Q_{ez} = -\frac{4\gamma^2}{A}\mathrm{Re}\sum_{j,m}(2j+1)(a_j+b_j)G_{j,m}(G'_{j,m})^*. \tag{C.4}$$

For the above expressions, $G_{j,m}$ and $G'_{j,m}$ are multipole coefficients of the focused beam:

$$G_{j,m}(\rho_R, z_R) = \int_0^{\theta_0} \mathrm{d}\theta \sin\theta\sqrt{\cos\theta}e^{-\gamma^2\sin^2\theta}d^j_{m,l}(\theta)J_{m-1}(k\rho_R\sin\theta)e^{ikz_R\cos\theta} \tag{C.5}$$

$$G'_{j,m}(\rho_R, z_R) = -i\frac{\partial G_{j,m}}{\partial(kz_R)}, \tag{C.6}$$

and $d^j_{m,m'}(\theta)$ are the matrix elements of finite rotations.

Fig. (C.1) shows the axial trapping force along the direction of laser propagation for a one micrometer sphere. Each curve is for a sphere with a different index of refraction. These curves show that for silica and polystyrene trapping in the z-direction is possible and will happen at about 100 nm past the focal point of the laser. For materials with a high index of refraction, such as ZnS, there is no stable trapping equilibrium. In those cases three-dimensional trapping is not possible.

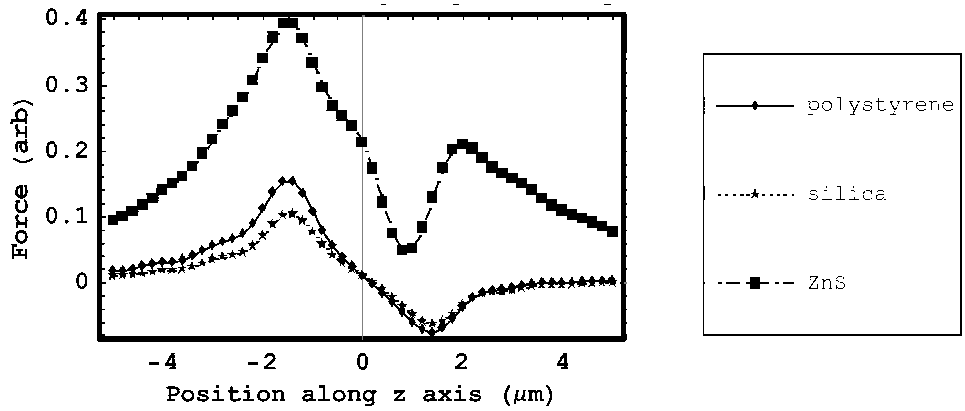

Figure C.1. These curves show the force on a 1 μm sphere in water due to an optical trap along the z-axis. The sphere would have a stable trapping equilibrium at the point of zero force. Zero on the z-axis represents the focal point of the laser. Because of the balancing of the radiation force and the gradient force, trapping equilibrium is shifted slightly in the positive direction of the z-axis. For polystyrene and silica the trapping equilibrium occurs at about 100 nm. For ZnS, index of refraction of 2.1, the force never reaches zero and there is no stable trapping point.

BIBLIOGRAPHY

[1] A. Yildiz, J. N. Forkey, S. A. McKinney, T. Ha, Y. E. Goldman, and P. R. Selvin, Science **300**, 2061 (2003).

[2] S. M. Block, Cell **93**, 5 (1998).

[3] P. Nelson, *Biological Physics: Energy, Information, Life* (W. H. Freeman and Company, 2004).

[4] A. Einstein, Annalen der Physik **8**, 549 (1905).

[5] R. D. Astumian and P. Hanggi, Phys. Today **55**, 33 (2002).

[6] R. P. Feynman, *Lectures in Physics*, vol. 1 (Addison-Wesley, 1963).

[7] P. Eshuis, K. van der Weele, D. Lohse, and D. van der Meer, Phys. Rev. Lett. **preprint** (2010).

[8] R. F. Fox, Phys. Rev. E **57**, 2177 (1998).

[9] S. Saffarian, H. Qian, I. Collier, E. Elson, and G. Goldberg, Phys. Rev. E **73**, 041909 (2006).

[10] R. Bartussek, P. Hänggi, and J. G. Kissner, Europhys. Lett. **28**, 459 (1994).

[11] T. Harada and K. Yoshikawa, Phys. Rev. E **69**, 031113 (2004).

[12] R. Astumian and M. Bier, Phys. Rev. Lett. **72**, 1766 (1994).

[13] J. Prost, J. Chauwin, L. Peliti, and A. Adjari, Phys. Rev. Lett. **72**, 2652 (1994).

[14] L. P. Faucheux, L. S. Bourdieu, P. D. Kaplan, and A. J. Libchaber, Phys. Rev. Lett. **74**, 1504 (1995).

[15] L. P. Faucheux, G. Stolovitzky, and A. Libchaber, Phys. Rev. E **51**, 5239 (1995).

[16] J. S. Bader, R. W. Hammond, S. A. Henck, M. W. Deem, G. A. McDermott, J. M. Bustillo, J. W. Simpson, G. T. Mulhern, and J. M. Rothberg, Proc. Natl. Acad. Sci. **96**, 13165 (1999).

[17] S. H. Lee and D. G. Grier, J. Phys: Condens. Matter **17**, S3685 (2005).

[18] P. Sjölund, S. J. H. Petra, C. M. Dion, S. Jonsell, M. Nylén, L. Sanchez-Palencia, and A. Kastberg, Phys. Rev. Lett. **96**, 190602 (2006).

[19] A. Ashkin, Proc. Natl. Acad. Sci. **94**, 4853 (1997).

[20] P. A. M. Neto and H. M. Nussenzveig, Europhys. Lett. **50**, 702 (2000).

[21] A. Mazolli, P. A. M. Neto, and H. M. Nussenzveig, Proc. R. Soc. Lond. A **459**, 3021 (2003).

[22] A. Rohrbach and E. H. K. Stelzer, J. Opt. Soc. Am. A **18**, 839 (2001).

[23] A. Rohrbach and E. H. K. Stelzer, Applied Optics **41**, 2494 (2002).

[24] A. C. Dogariu and R. Rajagopalan, Langmuir **16**, 2770 (1999).

[25] J. R. Moffitt, Y. R. Chemla, S. B. Smith, and C. Bustamante, Annu. Rev. Biochem **77**, 205 (2008).

[26] G. Volpe, G. P. Singh, and D. Petrov, Appl. Phys. Lett. **88**, 231106 (2006).

[27] M. Wei, K. Yang, A. Karmenyan, and A. Chiou, Optics Express **14**, 3056 (2006).

[28] J. E. Reiner, A. M. Crawford, R. B. Kishore, L. S. Goldner, K. Helmerson, and M. K. Gilson, Appl. Phys. Lett. **89**, 013904 (2006).

[29] R. Nambiar, A. Gajraj, and J. C. Meiners, Biophys. J. **87**, 1972 (2004).

[30] J. W. J. Kerssemakers, E. L. Munteanu, T. L. Noetzel, M. E. Janson, and M. Dogterom, Nature **442**, 709 (2006).

[31] E. A. Abbondanzieri, W. J. Greenleaf, J. W. Shaevitz, R. Landick, and S. M. Block, Nature **438**, 460 (2005).

[32] N. J. Carter and R. A. Cross, Nature **435**, 308 (2005).

[33] S. M. Block, Biophys. J. **92**, 2986 (2007).

[34] A. E. M. Clemen, M. Vilfan, J. Jaud, J. Zhang, M. Bährmann, and M. Rief, Biophys. J. **88**, 4402 (2005).

[35] C. Veigel, S. Schmitz, F. Wang, and J. R. Sellers, Nature Cell Biology **7**, 861 (2005).

[36] S. Toba, T. M. Watanabe, L. Yamaguchi-Okimoto, Y. Y. Toyoshima, and H. Higuchi, Proc. Natl. Acad. Sci. **103**, 5741 (2006).

[37] M. J. I. Müller, S. Klumpp, and R. Lipowsky, Biophys. J. **98**, 2610 (2010).

[38] Y. Roichman and D. G. Grier, Optics Letters **31**, 1655 (2006).

[39] Y. Roichman, V. Wong, and D. G. Grier, Phys. Rev. E **75**, 011407 (2007).

[40] L. Holzer, J. Bammert, R. Rzehak, and W. Zimmermann, Phys. Rev. E **81**, 041124 (2010).

[41] C. Lutz, M. Kollmann, P. Leiderer, and C. Bechinger, J. Phys.: Condens. Matter **16**, S4075 (2004).

[42] P. L. Biancaniello and J. C. Crocker, Rev. of Sci. Instr. **77**, 113702 (2006).

[43] G. T. Tietjen, Y. Kong, and R. Parthasarathy, Opt. Express **16**, 10341 (2008).

[44] Y. Kong and R. Parthasarathy, Soft Matter **9**, 2027 (2009).

[45] J. C. Crocker, J. A. Matteo, A. D. Dinsmore, and A. G. Yodh, Phys. Rev. Lett. **82**, 4352 (1999).

[46] C. Lutz, M. Kollmann, and C. Bechinger, Phys. Rev. Lett. **93**, 026001 (2004).

[47] B. Liesfeld, R. Nambiar, and J. C. Meiners, Phys. Rev. E **68**, 051907 (2003).

[48] E. M. Craig, B. R. Long, J. M. R. Parrondo, and H. Linke, Europhys. Lett. **81**, 10002 (2008).

[49] F. J. Cao, L. Dinis, and J. M. R. Parrondo, Phys. Rev. Lett. **93**, 040603 (2004).

[50] L. Dinis, J. M. R. Parrondo, and F. J. Cao, Europhys. Lett. **71**, 536 (2005).

[51] E. M. Craig, N. J. Kuwada, B. J. Lopez, and H. Linke, Ann. Phys. **17**, 115 (2008).

[52] M. Feito and F. J. Cao, Phys. Rev. E **76**, 061113 (2007).

[53] M. Feito and F. J. Cao, Physica A **383**, 4553 (2008).

[54] M. Feito and F. J. Cao, Europhys. Journ. B **59**, 63 (2007).

[55] F. J. Cao, M. Feito, and H. Touchette, Physica A **388**, 113 (2009).

[56] D. Voet and J. G. Voet, *Biochemistry, 3rd edition* (Wiley, 2004).

[57] H. Itoh, A. Takahashi, K. Adachi, H. Noji, R. Yasuda, M. Yoshida, and K. K. Jr., Nature **427**, 465 (2004).

[58] M. Schliwa and G. Woehlke, Nature **422**, 759 (2003).

[59] N. R. Guydosh and S. M. Block, PNAS **103**, 80548059 (2006).

[60] C. Veigel, F. Wang, M. L. Bartoo, J. R. Sellers, and J. E. Molloy, Nature Cell Biology **4**, 59 (2002).

[61] G. Cappello, P. Pierobon, C. Symonds, L. Busoni, J. Christof, M. Gebhardt, M. Rief, and J. Prost, Proceedings of the National Academy of Sciences **104**, 15328 (2007).

[62] E. M. Craig and H. Linke, Proc. Natl. Acad. Sci. **106**, 18261 (2009).

[63] R. Feynman, Phys. Today **42** (1989).

[64] J. Bath and A. J. Turberfield, Nature Nanotech. **2**, 275 (2007).

[65] R. Pei, S. K. Taylor, D. Stefanovic, S. Rudchenko, T. E. Mitchell, and M. N. Stojanovic, J. Am. Chem. Soc. **39**, 12693 (2006).

[66] S. J. Green, J. Bath, and A. J. Turberfield, Phys. Rev. Lett. **101**, 238101 (2008).

[67] T. Omabegho, R. Sha, and N. C. Seeman, Science **67**, 67 (2009).

[68] E. H. C. Bromley, N. J. Kuwada, M. J. Zuckermann, R. Donadini, L. Samii, G. A. Blab, G. J. Gemmen, B. J. Lopez, P. M. G. Curmi, N. R. Forde, et al., HFSP Journal **3**, 204 (2009).

[69] W. Reisner, J. P. Beech, N. B. Larsen, H. Flyvbjerg, A. Kristensen, and J. O. Tegenfeldt, Phys. Rev. Lett. **99**, 058302 (2007).

[70] L. Finzi and J. Gelles, Science **267**, 378 (1995).

[71] D. A. Schafer, J. Gelles, M. P. Sheetz, and R. Landick, Nature **352**, 444 (1991).

[72] H. Yin, R. Landick, and J. Gelles, Biophys. J. **67**, 2468 (1994).

[73] J. Carey, Proc. Natl. Acad. Sci. U.S.A. **85**, 975 (1988).

[74] K. L. B. Borrden, P. Beckmann, and A. N. Lane, Eur. J. Biochem **202**, 459 (1991).

[75] K. Phillips and S. E. Phillips, Structure (London) **2**, 309 (2007).

[76] X. S. Xie and H. P. Lu, J. of Bio. Chem. **274**, 15967 (1999).

[77] Y. Wang, J. Y. Shyy, and S. Chien, Annual Review of Biomedical Engineering **10**, 1 (2008).

[78] C. K. O'Sullivan and G. G. Guilbault, Biosensors and Bioelectronics **14**, 663 (1999).

[79] S. Tombelli, M. Minunni, and M. Mascini, Methods **37**, 48 (2005).

[80] E. A. Bayer and T. K. Christopoulos, *The avidin-biotin system* (Academic Press, Inc., 1996).

[81] A. T. Marttila, O. H. Laitinen, K. J. Airenne, T. Kulik, E. A. Bayer, M. Wilchek, and M. S. Kulomaa, FEBS Letters **467**, 31 (2000).

[82] H. R. Petty, Microscopy Research and Technique **70**, 687 (2007).

[83] D. E. Segall, P. C. Nelson, and R. Phillips, Phys. Rev. Lett. **96**, 088306 (2006).

[84] A. E. Knight, C. Veigel, C. Chambers, and J. E. Molloy, Prog. in Biophys. and Mol. Bio. **77**, 45 (2001).

[85] Y. Okada and N. Hirokawa, Science **283**, 1152 (1999).

[86] M. Bier, BioSystems **88**, 301 (2004).